Superconducting kinetic inductance bolometer focal plane array for passive terahertz imaging system

Lehtisyrjä, Lassi

Published: 13/08/2021

Document Version
Publisher's final version

Please cite the original version:
Lehtisyrjä, L. (2021). *Superconducting kinetic inductance bolometer focal plane array for passive terahertz imaging system*. Lappeenranta University of Technology. https://urn.fi/URN:NBN:fi-fe2021081343238

Lappeenranta-Lahti University of Technology LUT
School of Engineering Science
Computational Engineering and Technical Physics
Technical Physics

Lassi Lehtisyrjä

SUPERCONDUCTING KINETIC INDUCTANCE BOLOMETER FOCAL PLANE ARRAY FOR PASSIVE TERAHERTZ IMAGING SYSTEM

Master's Thesis

Examiners: Professor Erkki Lähderanta
D.Sc. Juho Luomahaara

Supervisors: D.Sc. Juho Luomahaara

ABSTRACT

Lappeenranta-Lahti University of Technology LUT
School of Engineering Science
Computational Engineering and Technical Physics
Technical Physics

Lassi Lehtisyrjä

SUPERCONDUCTING KINETIC INDUCTANCE BOLOMETER FOCAL PLANE ARRAY FOR PASSIVE TERAHERTZ IMAGING SYSTEM

Master's Thesis

2021

87 pages, 33 figures, 6 tables, 1 appendix.

Examiners:	Professor Erkki Lähderanta D.Sc. Juho Luomahaara

Keywords: terahertz, sub-millimeter wave, detector, imaging, concealed object detection, security screening, superconducting, kinetic inductance, bolometer, resonator, focal plane array, niobium nitride, critical temperature, two-fluid model, Mattis-Bardeen theory, quantum technology

The demands for high performance concealed object detection in mass transit, public events or industrial facilities have been increasing in light of increased risks. Concealed object detection at high throughput rates in places where lives can be jeopardized or where there is a risk of smuggling prohibited objects is a major challenge using conventional methods. Terahertz radiation has attracted attention for utilization in security imaging applications, due to its ability to penetrate dielectric materials, such as common clothing and packaging materials, while being strongly reflected from metals and strongly absorbed by water. Terahertz radiation also strongly interacts with organic matter, enabling spectroscopic techniques for the detection of explosives and narcotics, for example. The utilization of terahertz imaging helps to solve the problems of conventional physical se-

curity requiring straight body human contact. Terahertz radiation is also inherently safe when compared to alternative technologies such as X-ray imaging, due to its non-ionising nature. The diffraction-limited spatial resolution of sub-millimeter wave imaging (in the order of 15 millimeters) does not reveal anatomical details, guaranteeing the privacy of the scanned people.

Meanwhile, ever cheaper, more compact and easier to use cryocoolers capable of reaching temperatures down to less than 10 Kelvin (-263 °C) enable the utilization of superconducting electronics and detectors. These low temperatures allow for much lower thermal noise in detectors when compared to their room temperature equivalents, enabling much higher sensitivity. These high sensitivity imaging detectors are able to operate passively, without the need for bulky, intrusive and expensive high-power coherent terahertz sources, detecting the natural thermal blackbody terahertz radiation. The low temperatures also allow exploiting superconducting materials and their phenomena, such as exceptionally low conduction losses and high kinetic inductance.

Enabled by modern microfabrication technologies, VTT's (Technical Research Centre of Finland) superconducting kinetic inductance bolometers provide a solution for implementing a large focal plane array of detector pixels, enabling a high-performance passive terahertz imaging system for security imaging of human-sized objects at a close range and video frame rates. The high responsivity and inherent multiplexability negate the need for expensive and complex cryogenic signal amplification or high-bandwidth RF components in the system.

In this thesis, the superconducting properties of these kinetic inductance bolometers were characterized as a function of their temperature and geographical location on the wafer and assessed considering the theoretical predictions of both the two-fluid and the Mattis-Bardeen models. Further measurements were made in an attempt to characterize the noise and thermal properties of the bolometers and to determine the superconducting parameters of the thin superconducting films. The obtained data provides the basis for understanding the performance of the detectors and improving the design and fabrication process for bolometers in the future.

TIIVISTELMÄ

Lappeenrannan-Lahden teknillinen yliopisto LUT
School of Engineering Science
Laskennallinen tekniikka
Teknillinen fysiikka

Lassi Lehtisyrjä

SUPRAJOHTAVIIN KINEETTISEN INDUKTANSSIN BOLOMETREIHIN PERUSTUVA DETEKTORIMATRIISI PASSIIVISEN TERAHERTSIKUVANTAMISEN TARPEISIIN

Diplomityö

2021

87 sivua, 33 kuvaa, 6 taulukkoa, 1 liite.

Tarkastajat:	Professori Erkki Lähderanta
	D.Sc. Juho Luomahaara

Avainsanat: terahertsi, alimillimetriaalto, detektori, kuvantaminen, piilotetun esineen tunnistus, turvatarkastus, suprajohtava, kineettinen induktanssi, bolometri, resonaattori, niobinitridi, kriittinen lämpötila, kaksinestemalli, Mattis-Bardeen-teoria, kvanttiteknologia

Vaatimukset korkean suorituskyvyn piilotettujen esineiden tunnistamiseen julkisessa liikenteessä, yleisötapahtumissa ja tuotantolaitoksissa ovat lisääntyneet kasvavien riskien vuoksi. Suuren ihmismäärän turvatarkastus paikoissa, joissa on riski kiellettyjen esineiden salakuljettamiseen tai henkilövahingoille on suuri haaste tavanomaisille menetelmille. Terahertsisäteily on kiinnittänyt paljon huomiota turvallisuussovelluksissa, sillä se kykenee läpäisemään eristäviä materiaaleja, kuten yleiset vaate- ja pakkausmateriaalit, samalla heijastuen voimakkaasti metalleista ja absorboituen voimakkaasti veteen. Terahertsisäteily vuorovaikuttaa voimakkaasti myös orgaanisten aineiden kanssa, mahdollistaen spektroskopiatekniikoiden käyttämisen esimerkiksi räjähteiden ja huumausaineiden tunnistamiseen. Terahertsikuvantaminen auttaa ratkaisemaan suoraa ihmiskontaktia vaativan

perinteisen fyysisen turvatarkastuksen ongelmia. Koska terahertsisäteily ei ole ionisoivaa, on se myös luonnostaan turvallista verrattuna vaihtoehtoisiin teknologioihin, kuten röntgenkuvantamiseen. Alimillimetrikuvantamisen diffraktiorajoitettu resoluutio (n. 15 mm) ei paljasta anatomisia yksityiskohtia, taaten yksityisuudenturvan kuvatuille kohteille.

Samanaikaisesti yhä edullisemmat, pienikokoisemmat ja helppokäyttöisemmät alle kymmenen Kelvinin (-263 °C) lämpötiloihin kykenevät kryojäähdyttimet mahdollistavat suprajohtavan elektroniikan ja detektorien käytön. Matalat lämpötilat tarkoittavat paljon pienempää lämpökohinaa, joten jäähdytetyt detektorit kykenevät paljon suurempaan herkkyyteen verrattuna huoneenlämmössä toimiviin vastineihinsa. Nämä suuren herkkyyden detektorit kykenevät toimimaan passiivisesti ilman tarvetta suurikokoiselle, häiritseville ja kalliille suuritehoisille koherenteille terahertsilähteille, sillä ne havaitsevat luonnollisen lämmöstä johtuvan mustan kappaleen terahertsisäteilyn. Matalat lämpötilat mahdollistavat suprajohtavien materiaalien ja niiden ominaisuuksien hyväksikäytön, kuten erittäin matalat johtavuushäviöt ja korkea kineettinen induktanssi.

Modernin mikrofabrikaatiotekniikan ansiosta Teknologian tutkimuskeskus VTT:n suprajohtavat kineettisen induktanssin bolometrit tarjoavat ratkaisun suuren detektorimatriisin valmistamiseen. Tämä mahdollistaa korkean suorituskyvyn passiivisen terahertsikuvantamisjärjestelmän, joka soveltuu ihmisen kokoisten kohteiden videokuvaamiseen lähietäisyydeltä turvatarkastustilanteessa. Detektoreiden korkean responsiviteetin ja luonnostaan helpon multipleksoinnin ansiosta järjestelmä ei tarvitse kalliita ja monimutkaisia kryogeenisiä vahvistimia tai laajakaistaisia radiotaajuuskomponentteja.

Tässä diplomityössä tutkittiin lämpötilan ja kiekolla sijainnin vaikutusta näiden kineettisen induktanssin bolometrien suprajohtaviin ominaisuuksiin ja verrattiin mitattuja tuloksia kaksinestemallin ja Mattis-Bardeen-teorian ennustuksiin. Mittauksia tehtiin myös bolometrien lämpö- ja kohinaominaisuuksien selvittämiseksi sekä ohuiden suprajohdekalvojen parametrien määrittämiseksi. Kerätty data antaa pohjan detektorien suorituskyvyn ymmärtämiseen sekä tulevaisuuden bolometrien suunnittelun ja valmistusprosessien parantamiseen.

PREFACE

I would like to thank VTT and the Quantum Hardware team for giving me the opportunity to stretch my legs in high impact research work and to work with groundbreaking technologies first-hand. Thank you to Juho for supervising my work and giving me the kick-start into the career of science. I am thankful for the trust put in me. Thank you to VTT Young Professionals for distracting me from actual work while getting to know some of the coolest people.

These past six years at Lappeenranta have been the high point of my life. I would like to thank the guild of computational engineering Lateksii ry, the music club TeMu ry, reservist club LaTeRes ry, Tekniikan Akateemiset TEK and the student union of Lappeenranta University of Technology LTKY for keeping me distracted from my studies and giving me the opportunity to be a part of making Lappeenranta the best place for a student to be and getting the chance to leave a lasting mark in the Lappeenranta student culture. The experiences and memories will be with me until the end.

I would like to thank Sari for being there when I needed a bunk for the night, feeding me or the car ride to a job interview. I would not be here today without your support.

And of course, my fiancée Patricia. Your company and support kept me going through the most difficult times while working on this thesis. Thank you for tolerating my nonsense. You are my love.

Thank you to all the friends I made along the way. A man may leave Lappeenranta, but Lappeenranta will never leave a man. Keep the sauna warm and the beer cold.

Dedicated to my parents, Kirsi and Harri. I made it.

Otaniemi, Espoo, August 13, 2021

Lassi Lehtisyrjä

CONTENTS

APPENDICES

LIST OF ABBREVIATIONS

ADC	analog-to-digital-converter
ALD	atomic layer deposition
CMB	cosmic microwave background
CMOS	complementary metal oxide semiconductor
DOF	depth of field
EHF	extremely high frequency
FDM	frequency division multiplexing
FIR	far-infrared
FOV	field of view
FPA	focal plane array
HEB	hot electron bolometer
KIB	kinetic inductance bolometer
KID	kinetic inductance detector
LNA	low noise amplifier
MMCX	micro-miniature coaxial
NEP	noise equivalent power
NETD	noise equivalent temperature difference
NLoS	non-line-of-sight
PCB	printed circuit board
PSD	power spectral density
PSF	point spread function
RCS	radar scattering signature
RF	radio frequency
SAFE	serial addressed frequency excitation
SNR	signal-to-noise ratio
SOI	silicon on insulator
SQUID	superconducting quantum interference device
TDM	time division multiplexing
TES	transition edge sensor
THz	terahertz
VNA	vector network analyser

LIST OF SYMBOLS

α_{kin}	Kinetic inductance fraction
Δf	Bandwidth
Δx	Spatial resolution
Δ	Gap energy of a superconductor
δ	Skin depth
$\Delta\omega$	Bandwidth of a resonator
ϵ	Emissivity/absorptivity
$\frac{P}{A}$	Radiated power per radiating area
$\hbar$	The reduced Planck constant $\left(\frac{h}{2\pi}\right)$
λ	Penetration depth
λ	Wavelength of radiation
λ_L	The London penetration depth
$\mathbf{B}$	Magnetic field
$\mathbf{E}$	Alternating electric field
$\mathbf{J}$	Current density
$\mathfrak{R}$	Responsivity
μ_0	The vacuum permeability ($1.2567 \cdot 10^{16}$ H/m)
ω	Angular frequency
ω_0	Resonant angular frequency
$\Psi(\mathbf{r}, t)$	A wavefunction
ρ_{RT}	Room temperature resistivity
σ	The Stefan-Boltzmann constant ($5.6703 \cdot 10^{-8}$ W/m^{2}K^4)
σ_1	The real component of Drude conductivity
σ_2	The imaginary component of Drude conductivity

σ_n	Drude conductivity of a normal metal
τ	Average time between electron scattering events
τ_F	Frame time
τ_S	Slot time
τ_{th}	Thermal time constant
ξ	Coherence length of a superconductor
C	Capacitance
C	Heat capacitance
E	Energy
e	Euler's number (2.7183)
e	The electron charge ($1.6022 \cdot 10^{-19}$ C)
E_e	Energy stored in the electric field
E_F	The Fermi energy
E_k	Kinetic energy density
E_m	Energy stored in the magnetic field
E_{stored}	Energy stored in an oscillator
f	Frequency
f_c	Thermal cut-off frequency
f_ch	Chopper frequency
f_r	Resonant frequency
f_s	Sampling rate
G	Thermal conductance
h	The Planck constant ($6.6261 \cdot 10^{34}$ J/Hz)
h_{bs}	Height of backshort cavity
I	Electrical current

j	The imaginary unit
k_B	The Boltzmann constant ($1.3806 \cdot 10^{-23}$ J/K)
L	Inductance
L_g	Geometric inductance
L_s	Surface inductance
L_{kin}	Kinetic inductance
m_e	Effective mass of an electron
N	Number of resonators in a readout channel
n	Total electron density
n_n	Density of normal electrons
n_s	Density of superconducting electrons
n_{qp}	Density of quasiparticles
P_{inc}	Incident radiation power
P_{loss}	Power dissipated due to losses
Q	Quality factor of an oscillator
Q_i	Intrinsic quality factor of an oscillator
R	Resistance
r	Reflectivity
R_s	Surface resistance
R_{ns}	Normal state sheet resistance
S_{21}	Transmission scattering parameter
T	Temperature of a radiating body
T	Temperature
t	Thickness of a superconducting film
t	Time

t	Transmission
T_b	Thermal bath temperature
T_c	Critical temperature of a superconductor
T_N	Noise temperature
V_C	Voltage of a capacitor
v_F	The Fermi velocity
v_n	Voltage noise
v_s	Drift velocity of superconducting electrons
V_{ext}	Excitation voltage
W	Width of a superconducting film
x_r	Fractional frequency shift
Z_0	Impedance of a transmission line
Z_{in}	Input impedance of a circuit

1 INTRODUCTION

Besides the primary usage in radio astronomy, terahertz (THz) imaging technology has very promising applications in the safety industry for people screening and detection of concealed contraband. The imaging system introduced in this thesis is especially useful for non-invasive surveillance of moving subjects, as it allows real-time video feed with a large field of view. The technology promises to be more cost-effective, faster, less intrusive, easier to deploy and inherently safe when compared to alternative technologies based on active THz imaging or X-rays. The system can be utilized for several applications, such as public transport, airports, event and VIP security, as well as loss prevention and industrial quality control. VTT (Technical Research Centre of Finland) has been developing detectors and instrumentation for sub-millimeter wave imaging for over 20 years, and the work has been commercialized by VTT spinoff Asqella Oy [1].

The sensitivity requirements for passive imaging favour the use of cryogenic detectors, allowing the exploitation of superconductor phenomena. The THz imaging system under study in this thesis is based on a focal plane array of superconducting kinetic inductance bolometers inside a cryostat with a transparent window for THz radiation. The bolometers are fabricated on a suspended nanomembrane on which the kinetic inductance of a superconducting thin film meander acts as the temperature transducer. The change in inductance is detected by a lumped element RLC radio frequency (RF) resonator. The radiation from the wide field of view is focused on the focal plane using a lens-based quasi-optical system. The cryostat operates at the temperature range of 4 to 9 Kelvin, cooled by a commercial closed-cycle Gifford-McMahon cryocooler. The readout of the focal plane array is achieved by room temperature excitation signal generation and readout electronics with transmission lines passing through the cold side of the cryostat. The electronics consist of time division multiplexing (TDM) RF resonance detection and temperature controller circuits. The demodulated signals captured from the resonance detection circuit are compiled into video images after post-processing.

1.1 Objectives and delimitations

The four main objectives of this thesis are the following:

1. Characterize superconductor parameters of the detectors in the imaging system by measuring the critical temperature T_c of the superconducting transition and the re-

sistivity of niobium nitride thin film samples. Use this data to determine their 0 Kelvin penetration depth $\lambda(0)$ and gap energy $\Delta(0)$.

2. Characterize the focal plane array of superconducting resonators with dispersive RF measurements. Calculate the kinetic inductance and quality factors of the resonators and asses the data with both the two-fluid and the Mattis-Bardeen models.

3. Measure the noise characteristics and the thermal cut-off frequency of the bolometers using a blackbody calibrator.

4. Calibrate the readout electronics and perform imaging experiments using the imaging system.

1.2 Structure of the thesis

In the first chapter, I introduce the concept of terahertz radiation and some applications, focusing particularly on terahertz imaging. I explain some technologies for generating and detecting terahertz radiation, the challenges facing the technology and the conception of cryogenic detectors for the commercial market.

In the second chapter, I delve into the theory of superconductivity, particularly the relevant phenomena to superconducting circuits. I explain briefly the concept of superconductivity. I introduce the concept of the complex conductivity in superconductors. I review the London and BCS theory to describe the relevant physics of superconductors. I introduce the two-fluid and Mattis-Bardeen models to describe the complex conductivity of a superconductor. I introduce the kinetic inductance phenomenon.

In the third chapter, I briefly review the theory of the radio frequency RLC resonator and its behaviour in circuits. I explain how the resonator parameters can be characterized by utilizing transmission measurements.

In the fourth chapter, I present the kinetic inductance bolometer, by first introducing the basic function of the bolometer as a radiation detector. Next, I explain the superconducting bolometer, its benefits and how the kinetic inductance can act as a temperature transducer.

In the fifth chapter, I present the terahertz imaging system under study, the LASTKID, and its components. I introduce some development background, the innovations, and the practicalities of imaging.

In the sixth chapter, I introduce the four experiments conducted as a part of this thesis. The first experiment is the measurement of the critical temperature and conductivity of the niobium nitride films in use in the focal plane array. In the second experiment, I conduct RF transmission measurements of the focal plane lumped element kinetic inductance bolometer (KIB) resonators. In the third experiment, I perform measurements to characterize the noise and thermal cut-off of the focal plane array bolometer using the system readout electronics. In the fourth experiment, the readout electronics are calibrated and imaging is performed with the system to verify its performance for concealed item detection.

In the two final chapters, I discuss the results of the current study, the implications, and needs for future study and draw my conclusions.

2 TERAHERTZ RADIATION

THz radiation is electromagnetic radiation, like visible light or radio waves. Although a clear definition does not exist in the literature, most sources define the terahertz band to be 0.1 to 10 THz (10^{12} Hz), between the microwave and infrared bands of the electromagnetic spectrum corresponding to wavelengths of approximately 3 mm to 30 µm and photon energies of 0.4 meV to 40 meV [2].

The THz band overlaps with its neighbouring spectral bands such as the millimeter wave band (Up to 300 GHz, also known as extremely high frequency (EHF)), the sub-millimeter wave band (0.3 to 3 THz) and the far-infrared (FIR) band (7.5 to 12 THz). These bands are also distinguished by their characteristic technologies, where traditionally millimeter wave emitters and sensors are solid-state devices based on microwave technologies while far-infrared applications rely on optical and thermal devices.

The THz region of the electromagnetic spectrum is crowded with phenomena from fundamental physical processes, such as rotational transitions of molecules, large-amplitude vibrational motions of organic compounds, lattice vibrations in solids, intraband transitions in semiconductors and energy gaps in superconductors. THz waves are also well known for their high absorption in water, the characteristics of which also vary over the three phases; vapour, liquid, and ice.

The main source of natural THz radiation is the thermal blackbody radiation emitted by all objects, as given by the Stefan-Boltzmann Law [3]

$$\frac{P}{A} = \sigma T^4 \tag{1}$$

where $\frac{P}{A}$ is the net radiated power per radiating area, σ the Stefan-Boltzmann constant ($5.6703 \cdot 10^{-8}$ $\mathrm{Wm}^{-2}\mathrm{K}^{-4}$) and T the temperature of the radiating body.

Even though the thermal emission of room temperature objects peaks in the near-infrared band (Fig. 1), the continuous blackbody spectrum has still significant energy down at THz frequencies.

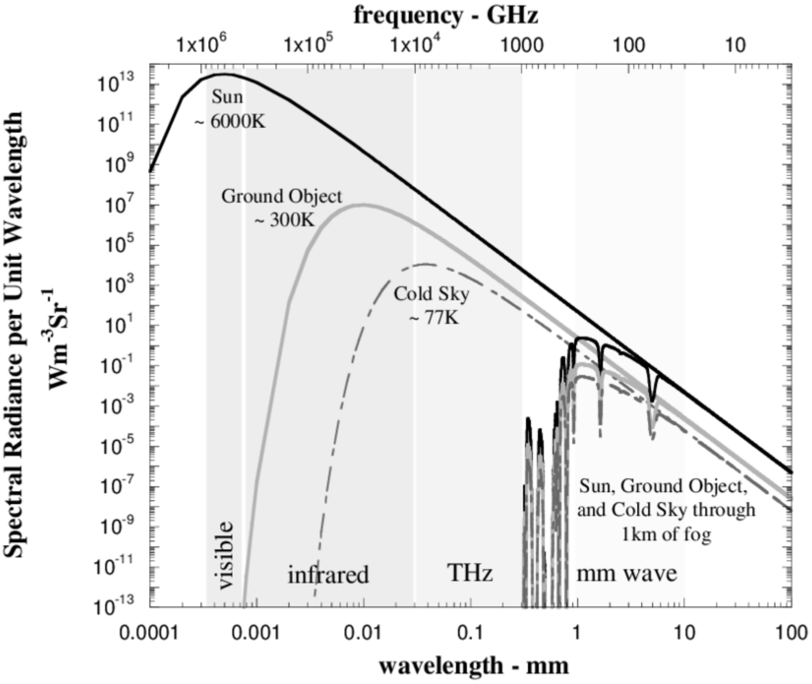

Figure 1. Blackbody radiation of objects at different temperatures [4].

The Universe itself acts also as a nearly perfect blackbody (Fig. 2). The cosmic microwave background (CMB) occupies the THz band peaking at 160.23 GHz, corresponding to a temperature of approximately 2.725 K.

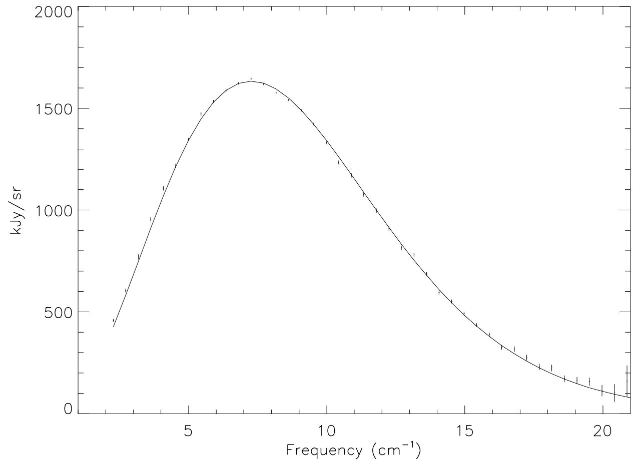

Figure 2. The cosmic microwave background as measured by the FIRAS instrument aboard COBE fitted with the Planck blackbody spectrum [5].

As the THz band is situated between the spectra covered by traditional electronics and optical technologies, the terahertz band has received the nickname "terahertz gap". While the traditional frequency bands have been thoroughly explored by science and engineering, the THz band has been relatively much less exploited as major challenges in technology have slowed down the development of applications. Currently, the lack of compact and inexpensive devices for generating and detecting THz radiation limits the interest for use in commercial applications.

A major challenge also in the terrestrial application of THz radiation is the high attenuation level in the Earth's atmosphere and the limits this sets to long-distance propagation. The rotational states of oxygen and water vapour in the air cause strong attenuation and specific spectral absorption/emission lines (Fig. 3).

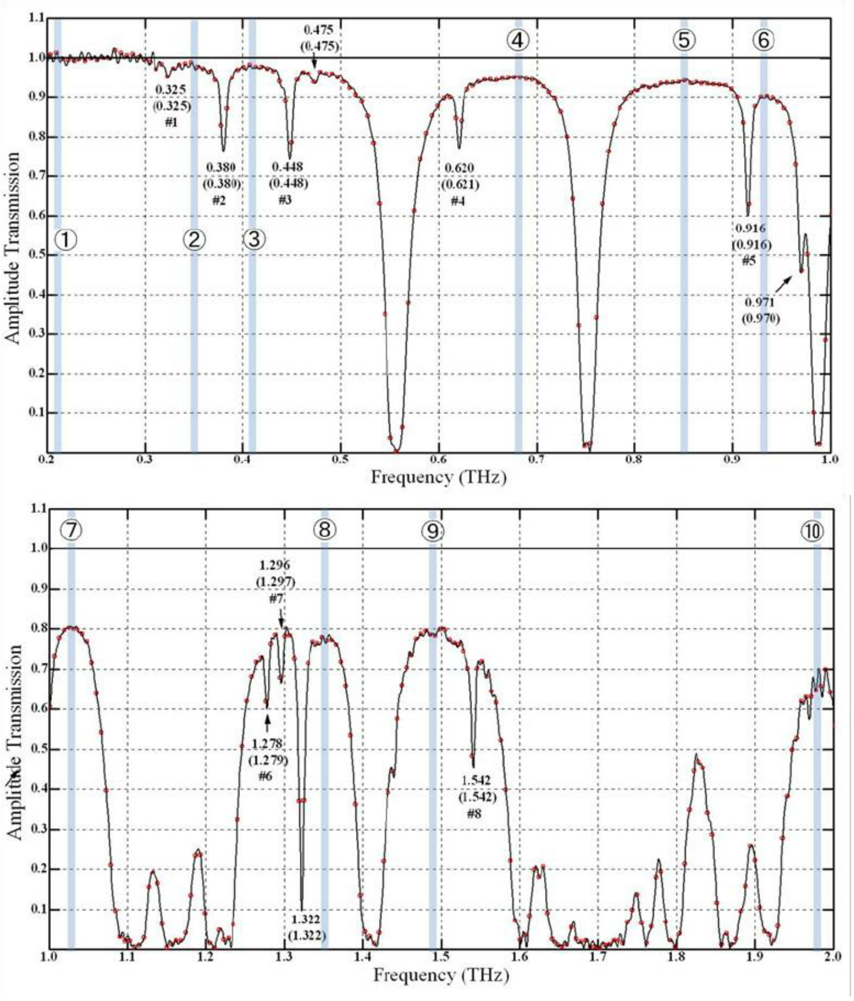

Figure 3. The amplitude transmission of 0.2 - 2 THz through 6.18 m of atmosphere at 21 °C with 51% relative humidity as measured by [6].

2.1 Applications of terahertz radiation

The interaction of terahertz radiation with many materials (especially organic compounds) and its relatively short wavelength leads to numerous possible applications, ranging from imaging, spectroscopy and astronomy to wireless communication and radar.

Spectroscopy at the THz frequency band is capable of analysing and detecting biological macromolecules such as amino acids, peptides, proteins, nucleic acids and carbohydrates. Spectroscopy techniques are particularly useful in the detection of explosives and narcotics, testing pharmaceutical products and investigating the conformation of proteins, as the complex organic compounds present cause distinctive absorption spectra [7].

Making astronomical observations in the sub-millimeter wave/THz band provides astronomers data about the fundamental structure of the Universe. For instance, the temperature distribution and polarity of the radiation of the cosmic microwave background reflects the conditions of the Universe present at the moment of the Big Bang, and the following inflation and cooldown. The CMB was released approximately 370000 years after the Big Bang when the Universe had cooled down enough for electrons and protons to form hydrogen atoms and therefore became transparent to electromagnetic radiation. The temperature fluctuations imprinted from the Big Bang onto the CMB describe the conditions present immediately after the Big Bang and their evolution to the present web of galaxy clusters and dark matter (Fig. 4). From these observations by the Planck satellite, researchers were able to determine in 2013 the age, composition, and the Hubble constant of the Universe [8].

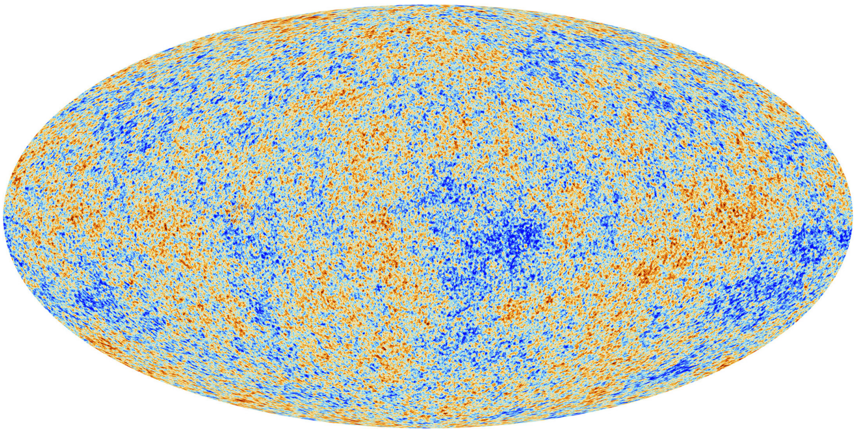

Figure 4. The CMB as observed by the Planck satellite [9].

The emission lines of many interesting biochemically relevant compounds also exist in the sub-millimeter wave band, such as water, oxygen, carbon monoxide and nitrogen. Sub-millimeter wave telescope satellites can observe the distribution and concentration of these compounds, indicating potential conditions for the creation of extraterrestrial life. Water and oxygen are the strongest absorbers of terahertz radiation in the Earth's atmosphere, meaning that planets with atmospheric conditions (temperature, pressure, and gas composition) suitable for life forms could be detected by sub-millimeter wave and terahertz spectroscopy [7].

Demand for ever faster wireless communication has driven the urge to investigate the terahertz band, as it combines good qualities from both the optical and radio frequency (millimeter wave) regimes. Higher bandwidths (up to terabits per second), higher link directionality and lower eavesdropping chances are achievable when compared to the millimeter wave band. THz enables non-line-of-sight (NLoS) propagation in comparison to optical frequencies and acts as a good substitute under inconvenient climate conditions such as fog, dust, and turbulence. In addition, the THz is not impacted by ambient noise arising from optical sources, nor is it associated with any health restrictions or safety limits [10].

Mobile applications are demanding higher resolution radar systems, especially in the automotive environment for use in autonomous driving sensor fusion systems. This has increased interest in terahertz band radars, as the shorter wavelength enables high resolution. In short-range applications (in the order of 1 meter), the atmospheric absorption of THz radiation is negligible, but the path loss caused by diffraction not. With an omnidirectional antenna, the roundtrip loss of the radar signal can be as high as 117 dB for a 100 cm radar cross-section object at a distance of 1 m. Therefore, the ability for beamforming and steering is invaluable. The lack of mainstay RF radar components in the THz band, such as phase shifters and circulators, currently limits these abilities [11].

While the main applications for THz radars are found in the automotive field, novel applications have emerged also in security, health monitoring, drones and human-computer interface fields. For example, non-contact vital sign monitoring is enabled with the higher resolution achievable with terahertz. A radar system can monitor the breathing and heartbeat of a patient from the tiny physiological movements induced. Such a device has multiple applications, for example, searching for survivors after earthquake disasters and monitoring sleeping infants or adults to detect abnormal breathing condition or vital patterns [12].

Terahertz radar can also be used as a tool for modelling the radar signatures of much larger objects, such as aircraft, tanks or naval vessels. With an appropriate scale model, the radar scattering signature (RCS) of the objects can be directly measured at the THz band, which correlates well with the life-size object's radar signature at conventional radar frequencies [7].

2.2 Sub-millimeter wave and terahertz imaging

THz band radiation offers great opportunities for terrestrial imaging systems in addition to the ones used in astronomy. Due to the shorter wavelength of the radiation, THz imagers are able to produce images with higher resolution than microwave imaging systems. Due to the non-ionizing nature of THz radiation, the increased safety of the technology when compared to X-rays has drawn great attention in for example in quality control, non-destructive evaluation, and medical and security applications (Fig. 5), as most dielectric materials are partially transparent at THz frequencies [7]. Terahertz radiation in these applications has also attained the nickname of T-Rays. Manipulation of THz radiation through optics, similar to visible light, can also be easily achieved.

Figure 5. A THz security scan image [13].

Terahertz imaging systems can be divided into two classes: active and passive. Passive imaging relies on the natural thermal blackbody radiation. Active systems rely on a system-provided high power THz radiation source and its reflection. Depending on the application, imaging systems of both modalities can operate on broadband sensors and non-coherent sources or be narrowed on specific spectral features.

In both active and passive scenarios, the response of the imaging target is dependent on its optical properties of emissivity/absorptivity (ϵ), reflectivity (r) and transmission (t). These quantities account for all the interaction of the material with the radiation, and as such obey the law $\epsilon + r + t = 1$. The combination of these parameters affects the apparent brightness of the imaging subject, depending on the thermal emission of the target, reflections from the surroundings and transmission from the background.

THz radiation can penetrate nonpolar and nonmetallic dielectric materials, such as paper, plastic, clothes, wood, and ceramics. Water, as a strongly polar liquid, is highly absorptive to THz radiation. Metals are highly reflective at THz frequencies due to their high electrical conductivity [14]. This strong contrast in the optical properties of materials is the key to enabling THz imaging. A detailed view of the optical properties of sub-millimeter radiation in the context of security applications is given in [15].

2.2.1 Technologies for terahertz detectors in imaging applications

As mentioned earlier, a technological gap in the terahertz frequency range gives rise to challenges for the detection of terahertz radiation.

Standard technologies in the optical regime are too insensitive to directly detect terahertz radiation, as the photon energy is too low to enable direct detection by way of exciting electrons over the bandgap in common semiconductor photosensors. Similarly, for coherent detection in solid-state components known from current radio frequency technologies, the high frequency of the terahertz band electromagnetic waves are too fast for them to respond. Heterodyne detection is the standard method for demodulating a high-frequency signal and bringing it down into usable intermediate frequency (IF) bandwidth. However, THz frequency local oscillators and mixers as well as low noise and high bandwidth IF amplifiers are required, which require state-of-the-art technologies to realize, confining them to laboratory and research environments [16].

For direct terahertz sensing, thermal sensors have become staple technology for direct detectors, where the impinging radiation power is detected by the temperature change caused by the absorption of energy in the sensor medium instead of electrical excitations. Heterodyne detectors are always limited in sensitivity by the fundamental quantum noise of mixers, whereas thermal detection does not suffer from this, reaching down to photon noise limited sensitivities. Such thermal sensors benefit greatly from operating at cryogenic temperatures, as this lowers the thermal noise, which is proportional to T^2. The low temperatures also enable the exploitation of superconducting phenomena, such as very low conduction losses, the gap energy Δ and the kinetic inductance L_{kin}. The advancements in cryogenic technology have brought affordable and compact cryocoolers to the market, which are capable of cooling detector systems to temperatures in the sub 10 Kelvin regime. Meanwhile, maturing wafer-level processes of thin superconducting films allow for the manufacture of complicated superconducting circuits on standard silicon wafers. Besides patterning, modern manufacturing processes allow readily modifying many of the critical parameters of superconducting materials. These factors have sparked interest in bringing commercial superconducting sensors and circuits to the market.

Here listed are a few superconducting terahertz detection technologies:

1. Hot electron bolometer (HEB) [17]: HEBs are constructed from a material with a weak electron-phonon coupling, for example, a thin film of a disordered superconductor such as niobium nitride (NbN), manifesting as a high resistivity in the normal state. For frequencies above the bandgap of the superconductor, the incoming radiation is absorbed by both single electrons (quasiparticles) and superconducting electrons (Cooper pairs). A change in the absorbed radiation power heats the electron system, causing a rapid change in the resistivity of the HEB device. The HEB is not only very sensitive to radiation but also extremely fast, as the thermal time constant is of the order tens of picoseconds, allowing a maximum detection signal frequency of several GHz. HEBs are usually realized as a superconducting microbridge coupled to a well conducting normal metal antenna.

2. Transition edge sensor (TES) [18]: A TES detects radiation by the temperature change caused by the absorption of radiation power in a thin superconducting film. The temperature change causes the film to transition from the superconducting state to the normal state. The film typically has a critical temperature of 0.1 to 0.4 K, and it is weakly thermally coupled to a lower bath temperature. The TES is self-heated to the vicinity of the superconducting transition by resistive heating by a voltage bias circuit. A temperature rise due to photon absorption causes a change in the resistance and therefore the current flowing through the TES.

3. Kinetic inductance detector (KID) [19]: In a KID, photons are absorbed directly by Cooper pairs in a superconducting film. If the energy of the photon surpasses

> the gap energy ($hf \geq 2\Delta$), the Cooper pair breaks apart. This increase in the population of quasiparticles increases the kinetic inductance of the sensor. This change is small and requires a sensitive readout, which be achieved by coupling the film to a high quality factor RF resonator and measuring the change in phase or amplitude of a microwave probe signal centred on the resonant frequency. The characteristic resonant frequency is easily tuned, meaning that large numbers of KIDs can be read out from a single transmission line by using frequency division multiplexing (FDM) scheme.

The common denominator for these technologies is that they operate at temperatures below 0.5 K, requiring the use of complex and expensive cryorefrigerators. To limit the thermal load of the cryostats, implementing an array of >10000 TES based THz detectors requires multiplexed readout usually realized with the superconducting quantum interference device (SQUID). SQUID based readout electronics are challenging and expensive to integrate on this scale due to the complexity of setting their operating point and their vulnerability to electromagnetic interference [20].

Kinetic inductance exploited in KIDs is also very sensitive to temperature, especially near the superconducting critical temperature of the material due to the steep gradient in the Cooper pair population. This can be exploited as the temperature transducer in a bolometric sensor, known as the KIB [21]. This is the core technology in the imaging system under study in this thesis and will be further discussed in the upcoming chapters.

2.2.2 Applications of terahertz imaging

The most prominent applications for terahertz imaging are found in radio astronomy and security. As discussed earlier in this chapter, observing the universe in the terahertz band presents a window into the early universe and a tool to probe the chemicals possibly involved in the creation of biological life.

However, in the scope of this thesis, the more mundane security application is the more relevant one.

For security applications, the use of terahertz technologies is motivated by multiple factors. The use of conventional methods for security screening, such as metal detectors and manual scanning, are no longer deemed secure enough in the light of current-day risks. Full-body X-ray scanning methods could provide the ability to scan for concealed items faster and without ambiguity, but questions on their privacy and health issues limit public acceptance. Terahertz imaging techniques bypass both of these issues, as the diffraction-limited resolution of terahertz images is not high enough to provide compromising pictures of a person's physique but still high enough for contraband detection. Health issues are also mitigated by not utilizing any forms of ionizing radiation.

THz radiation is able to penetrate clothing materials, while due to the high absorption coefficient of water the human body resembles a nearly perfect black body. This allows for a technique called passive imaging, which is able to provide thermal images of the temperature distribution on the body surface. Against the background of the radiating human body, different objects are visible due to the contrast in their radiometric brightness temperature. Hence, objects concealed under clothing can be detected. This applies to metals, which are highly reflective, ceramic materials and even explosives (exhibiting distinctive absorption spectra in the sub-millimeter range). A thorough overview of this application of sub-millimeter radiation is given in [15].

Active THz video cameras operate by illuminating the targets with high power radiation sources, making the detection with room temperature detectors adequate. Complex and physically large optics are required for shaping and focusing the radiation, as well as imaging human-sized objects at such a close range.

Transmission through dielectric materials decreases with increasing frequency. Attenuation in clothing and the atmosphere imposes an effective upper limit of 1 THz to the frequency band of interest for security applications [15]. Requirements for spatial resolution limit the usability of longer wavelengths for concealed item detection due to the fundamental diffraction limit, effectively limiting the lower end of the spectrum to a few hundred gigahertz.

In the light of the novel coronavirus pandemic of COVID-19, the safe distance non-contact and high throughput security checkup enabled by sub-millimeter wave imaging has attracted more attention to utilizing the technology. Accurate body temperature sensing for the detection of feverish persons has also increased attention in sub-millimeter waves as a tool for counter-pandemic applications. Compared to the more conventional infrared thermal imaging, the sub-millimeter wave thermal emission can be detected from underneath the person's clothing, while infrared band imaging is limited to measuring only the visible skin of the person (such as the face). The face is highly susceptible to temperature fluctuations caused by external factors, while the signal measured through the clothes is immune to this issue [22].

3 PHYSICS OF SUPERCONDUCTIVITY

All elemental metals exhibit a decrease in electrical resistance as the temperature decreases. In 1911 however, the Dutch physicist Heike Kamerlingh Onnes discovered that a sample of mercury cooled with liquefied helium reached an immeasurably small resistance [23]. The same phenomenon was later also observed in other metals such as niobium, lead, and aluminium. These materials are now known as superconductors. Each material undergoes the transition to the superconducting state when the temperature falls below their characteristic critical temperature T_c.

Superconductivity is not purely just perfect conductivity as bulk superconductors also exhibit perfect diamagnetism, called the Meissner effect, meaning that all magnetic flux density from the inside of the material will be expelled by induced surface currents. In the presence of external magnetic fields, a perfect conductor would also exhibit the same screening currents, preventing the field from penetrating the bulk of the conductor. This would imply that if a superconductor simply had perfect conductivity, a sample cooled below its critical temperature in a magnetic field would sustain the field within the bulk when the field was removed, due to the induced screening currents. A superconductor will completely expel all flux from its bulk interior, which implies a fundamental difference from a perfect conductor [24].

Superconductivity is an inherently quantum mechanical phenomenon observable on the macroscopic scale. Below the temperature of the superconducting phase change, electrons in the material form pairs of superconducting electrons known as Cooper pairs, which behave as a single quantum mechanical entity. The behaviour of all the superconducting electrons can be described with a single macroscopic wave function $\Psi(\mathbf{r}, t)$. The Cooper pairs are bound together by a pairing energy 2Δ, known as the gap energy, i.e., the energy required to break apart the Cooper pairs. The unpaired normal electrons in the superconductor are also known as quasiparticles [25].

3.1 Conductivity of normal metals

In a normal metal, electric current can be thought of as a fluid of electrons moving across a lattice of heavy ions. The electrons constantly collide with the ions in the lattice and lose some of their energy as heat, the vibrational kinetic energy of the lattice. Therefore, the energy carried by the electrical current is constantly dissipating, manifesting itself as electrical resistance and Joule heating.

The conductivity of normal metals is described by the Drude model [26]

$$\sigma_n = \frac{\sigma_0}{(1 - j\omega\tau)} \tag{2}$$

where j is the imaginary unit and $\sigma_0 = n_n e^2 \tau / m_e$, where n_n is the electron density (the notation n_n used to distinguish normal electrons from superconducting ones), e the electron charge, τ the average time between scattering events, m_e the electron effective mass and ω the angular frequency.

When separated into its real and imaginary components, the Drude conductivity takes the form

$$\sigma_n = \sigma_1 - j\sigma_2 = \frac{n_n e^2 \tau}{m_e(1 + \omega^2\tau^2)} - j\frac{n_n e^2 \tau^2 \omega}{m_e(1 + \omega^2\tau^2)} \tag{3}$$

The imaginary component of the conductivity (analogous to the reactance of circuit elements) arises due to the momentum of the electrons. In an alternating electric field, the velocity of the electrons doesn't change instantaneously, but over the time of τ. However, in normal metals at room temperature, the value of τ is so short (approximately 10^{-14} to 10^{-15} s) that the imaginary component is negligible until the frequency of the electric field reaches values in the terahertz range.

However, in a superconductor, superconducting electrons paired into Cooper pairs can travel through the medium without scattering and losing kinetic energy. But similar to normal electrons, the Cooper pairs have a finite momentum and cannot respond to changes in the electric field instantaneously. This gives rise to the phenomenon of the kinetic inductance. To understand kinetic inductance and its dependencies, we must describe the phenomenon in terms of superconductor electrodynamics.

3.2 Two-fluid model and the London model of superconductivity

In 1934 Gorter and Casimir constructed a phenomenological model of superconductivity known as the two-fluid model, mainly to describe the thermodynamic properties of superconductors [27]. In the two-fluid model, the electrons of a superconductor exist in two distinct populations: quasiparticles (i.e., normal, unbound electrons) and superconducting electrons (Cooper pairs).

The model describes the ratio of the electron population by

$$\frac{n_s}{n} = 1 - \left(\frac{T}{T_c}\right)^4 \tag{4}$$

where n is the total electron density $n = n_{qp} + n_s$, n_s the density of superconducting electrons and n_{qp} the density of quasiparticles (i.e., normal electrons).

At that time, the value of 4 for the exponent gave the best fit to experimental data observed from all known low-temperature superconducting materials, such as lead (Pb) and tin (Sn). More recently, with the discovery of high-temperature superconductors, such as yttrium barium copper oxide (YBCO), the observed data from penetration depth experiments for these materials show better agreement with the exponent value of 2 [28].

By utilizing the two-fluid model, London & London were able to mathematically describe the electrodynamics of a superconductor by applying Maxwell's equations, giving birth to the famous London model of superconductivity in 1935 [29]. The London model assumes that the electrons responsible for superconductivity do not scatter as they would in normal metal, therefore an alternating electric field ($\mathbf{E} = E_0 e^{j\omega t}$) accelerates the superconducting electrons without hindrance. This leads to the first London equation describing the perfect conductivity of a superconductor

$$\frac{d\mathbf{J}}{dt} = \frac{n_s e^2}{m_e}\mathbf{E} \tag{5}$$

Relating Eq. (5) to Ohm's law, which describes the relation of the electric field and current density in normal metals ($\mathbf{J} = \sigma\mathbf{E}$), gives us the conductivity of the superconducting electrons. The same result can be obtained from Eq. (3) by letting $\tau \to \infty$

$$\sigma_s = -j\frac{n_s e^2}{\omega m_e} \tag{6}$$

By applying this result to the Drude model of conductivity, the complex conductivity for a superconductor can be derived as

$$\sigma_{tot} = \frac{n_{qp}e^2\tau}{m_e(1+\omega^2\tau^2)} - j\left(\frac{n_s e^2}{m_e\omega} + \frac{n_{qp}e^2\tau^2\omega}{m_e(1+\omega^2\tau^2)}\right) \tag{7}$$

This is an important result for the two-fluid model, as it describes how the real (resistive) component of the conductivity is purely due to the normal electron population whereas the imaginary (inductive) component is a combination of both the normal and the superconducting electrons. The equivalent circuit is depicted in Fig. 6.

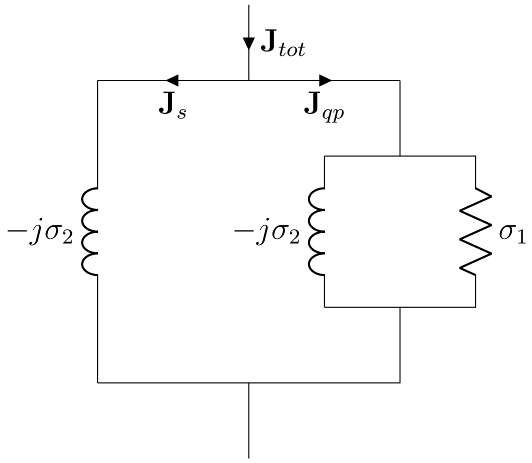

Figure 6. Equivalent circuit of the conductivity of a superconductor.

London & London also explained the Meissner effect through Maxwell's equation for Faraday's law of induction and Ampères circuital law

$$\nabla \times \mathbf{E} = -\frac{\partial \mathbf{B}}{\partial t} \tag{8}$$

$$\nabla \times \mathbf{B} = \mu_0 \left(\mathbf{J} + \frac{\partial \mathbf{E}}{\partial t}\right) \tag{9}$$

where $\mathbf{B}$ is the magnetic field and μ_0 is the vacuum permeability ($1.256637{\cdot}10^{-16}$ H/m).

When Eqs. (8) and (9) are applied to a perfect conductor, the result shows that the conductor will form screening currents to prevent the magnetic field from changing within its bulk

$$\frac{\partial \mathbf{B}}{\partial t}(x) = \frac{\partial \mathbf{B}}{\partial t}(a) \exp\left(\frac{-x}{\sqrt{m_e/\mu_0 n_s e^2}}\right) \tag{10}$$

where x is the distance from the conductor surface and $\frac{\partial \mathbf{B}}{\partial t}(a)$ the time-varying magnetic field at the surface of the conductor.

As per the Meissner effect, $\mathbf{B}$ inside the superconductor must be zero. London & London proposed a model through which both $\frac{\partial \mathbf{B}}{\partial t}$ and $\mathbf{B}$ can decay when moving inside from the surface of the superconductor. This means that Eq. (10) takes the form

$$\mathbf{B}(x) = \mathbf{B}(a) \exp\left(\frac{-x}{\sqrt{m_e/\mu_0 n_s e^2}}\right) \tag{11}$$

The field penetrating inside the surface of the superconductor decays to $1/e$ of its magnitude over the distance of λ_L, the London penetration depth.

$$\lambda_L = \sqrt{\frac{m_e}{\mu_0 n_s e^2}} \tag{12}$$

The London penetration depth also explains how screening currents induced by external magnetic fields do not cause an infinite current density at the surface of the superconductor, as the screening currents will occur inside the penetration depth.

Noting that the penetration depth in Eq. (12) has a dependency on n_s, we can derive the temperature dependency of the London penetration depth by utilizing Eq. (4).

$$\lambda_L(T) = \lambda_L(0) \left[1 - \left(\frac{T}{T_c}\right)^4\right]^{-\frac{1}{2}} \tag{13}$$

For a full derivation of the London equations, please see appendix of [30]. It must be also noted that the London equations do not address any of the fundamental microscopic physics of superconductors, but are rather a set of phenomenological relations that can be used to describe the experimentally observed effects. As the assumption of non-scattering superconducting electrons is not correct due to the finite size of Cooper pairs, a microscopic theory of superconductivity to accurately describe the complex conductivity of superconductors is required.

3.3 BCS theory

Bardeen, Cooper and Schrieffer proposed the microscopic theory of superconductivity in 1957 [31]. Known as the BCS theory, the theory asserted the existence of an energy gap and that the superconducting phenomena are the result of the pairing of two electrons with equal and opposite momenta and spins to form a Cooper pair with the binding energy of 2Δ. Cooper demonstrated that in a system of electrons at zero Kelvin where all the electron states up to the Fermi level (E_F) are filled, additional electrons (which would otherwise have energy $E > E_F$) could form a bound state with energy less than $2E_F$ if there existed even a weak attractive force between the electrons. This force results from the interaction of the electrons with the surrounding crystal lattice vibrations; phonons.

Interaction between the electrons forming a Cooper pair takes place over an average distance, the coherence length ξ. The coherence length at 0 Kelvin is given by [32] as

$$\xi(0) = \frac{0.18\hbar v_F}{k_B T_c} \tag{14}$$

where v_F is the Fermi velocity of the material. The coherence length is material dependent, as seen from the dependence on T_c and v_F, and is of the order 1 µm. This leads to the conclusion that the force on a Cooper pair cannot be simply described by the local electric field. A similar phenomenon occurs also in normal conductors, where the electron mean free path becomes comparable to the classical skin depth δ. This is known as the anomalous skin effect.

The BCS theory has been constructed with the constraint of the so-called dirty limit, where the electron mean free path l is much shorter than the coherence length $\xi(0)$. Accordingly, the penetration depth λ needs to be much shorter than $\xi(0)$.

The binding energy of the Cooper pair changes as a function of temperature (Fig. 7). BCS theory predicts this energy, depending on the critical temperature T_c [33]

$$\Delta(T) = \Delta(0) \tanh \left(1.74 \sqrt{\frac{T_c}{T} - 1} \right) \tag{15}$$

where $\Delta(0)$ is gap energy at absolute zero, predicted by BCS theory as

$$\Delta(0) = 1.76 k_B T_c \tag{16}$$

where k_B is the Boltzmann constant ($1.380649 \cdot 10^{-23}$ J/K).

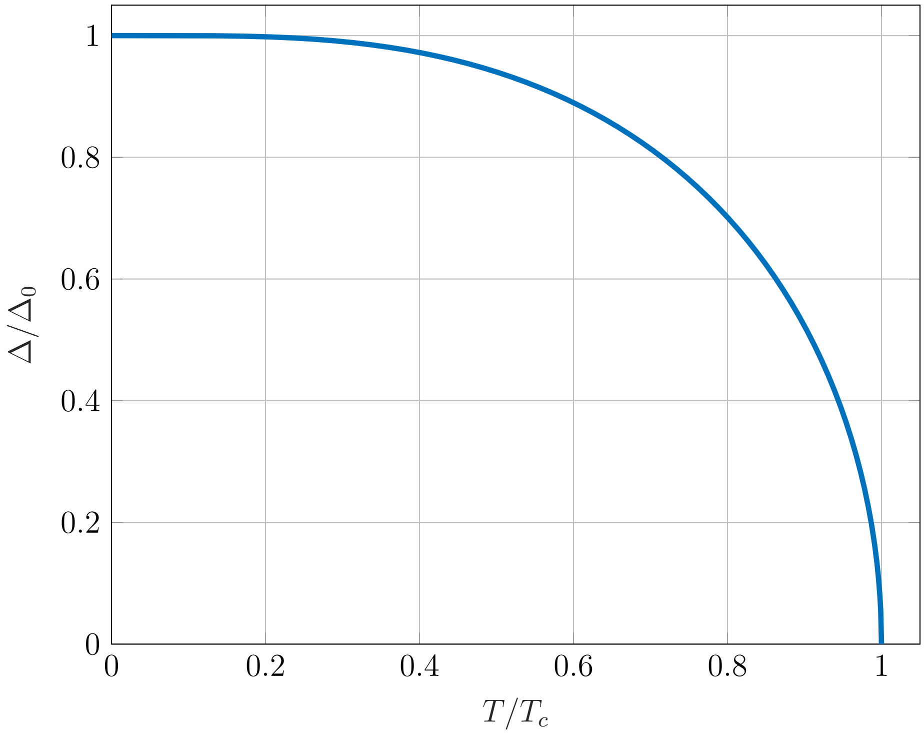

Figure 7. The temperature dependency of the energy gap Δ expressed as a function of T/T_c (Eq. (15)).

Mattis and Bardeen based their quantification of the complex conductance of superconductors on the BCS theory which, compared to the two-fluid model, accounts for the formation of Cooper pairs and quasiparticle excitations through the existence of the energy gap. When electrical fluctuations reach high enough energies ($\hbar\omega > 2\Delta$), the two-fluid model cannot predict the excess population of generated quasiparticles. The Mattis-Bardeen theory is therefore based on fundamental principles of superconductivity and not on phenomenological models from experimental observations.

The Mattis-Bardeen theory gives the complex conductivity of a superconductor as integrals [34]. See appendix 1 for the expressions. The integrals also introduce the Cooper pair breaking limit 2Δ, where a direct absorption of a photon has enough energy ($E = \hbar\omega$) for pair breaking. This sets the boundary where the integral limits switch. For materials relevant to this thesis, the limit is in the range $\Delta(0)/h \approx$ 90 - 500 GHz.

The dependency of the gap energy on the temperature directly affects the value of the penetration depth as well. The penetration depth according to the Mattis-Bardeen at low frequencies is given by the analytical expression [25]

$$\lambda(T) = \lambda(0) \left[\frac{\Delta}{\Delta(0)} \tanh\left(\frac{\Delta}{2k_B T} \right) \right]^{-\frac{1}{2}} \tag{17}$$

3.4 Inductance of superconducting thin films

The inductance of a superconducting film is the sum of its kinetic inductance L_{kin} and the geometric inductance L_g. As mentioned earlier, the kinetic inductance arises from the momentum of the superconducting electrons, while the geometric inductance is associated with the energy stored in a magnetic field. When the superconducting film is thin enough, energy can additionally be transferred between the motion of the Cooper pairs and the magnetic field, since magnetic fields penetrate below the surface of the superconductor to a distance of λ. This transfer of energy results in the surface kinetic inductance of the superconductor, which can dominate the total inductance over the inductance caused by the geometry of the circuit [35].

The kinetic inductance in a thin superconducting strip can be calculated by considering the kinetic energy density E_k of the superconducting electrons contributing to a current density J_s.

$$E_k = \frac{1}{2} n_s m_e v_s^2 = \frac{1}{2} \frac{m_e}{n_s e^2} J_s^2 = \frac{1}{2} \mu_0 \lambda^2 J_s^2 \tag{18}$$

where v_s is the drift velocity of the superconducting electrons.

Equating this kinetic energy to the total energy stored in the kinetic inductance ($\frac{1}{2} L_{kin} I^2$), we can determine the kinetic inductance.

$$U_k = \frac{1}{2} L_{kin} I^2 = \frac{1}{2} \mu_0 \lambda^2 \int_s J_s^2 \, ds \tag{19}$$

where U_{kin} is the kinetic energy per unit length and I the total current in the film. The surface integral performed over the cross-section of the film takes into account non-uniform current distribution.

In a thin film with the thickness t and the width W, where $t \ll \lambda \ll W$, the expression can be simplified, as the current density flows throughout the full cross-sectional area of the film, leading to $J_s = I/Wt$. The kinetic inductance by unit length is therefore given by

$$\frac{1}{2} L_{kin} I^2 = \frac{\mu_0 \lambda^2 I^2}{2 W^2 t^2} W t \tag{20}$$

$$L_{kin} = \frac{\mu_0 \lambda^2}{W t} \tag{21}$$

4 RADIO FREQUENCY RESONATOR THEORY

An RF resonator is a device that exhibits resonance behaviour at the radio frequencies of the electromagnetic spectrum. Resonance in the device exhibits as an increase in the amplitude of oscillation at a certain frequency, called the resonant frequency. RF resonators can take a variety of forms, including cavities, transmission lines and distributed element resonators. In the context of this thesis, I shall focus my attention on the lumped element RLC resonator.

4.1 The lumped element RLC resonator

An RLC circuit is a circuit consisting of a resistor (R), an inductor (L), and a capacitor (C) connected in series (Fig. 8) or parallel. In resonance, the RLC circuit forms a harmonic oscillator for electrical current. The lumped element resonator model means that the spatially distributed impedance characteristics of a resonator system are simplified to discrete electrical circuit elements. Such a simplification is justified when the characteristic electrical length of the circuit is much shorter than the wavelength of the signals in the circuit, i.e., the voltage and current do not vary appreciably over the physical dimension of the circuit elements [36]. For example, the wavelength of a 200 MHz signal is approximately 1.5 m.

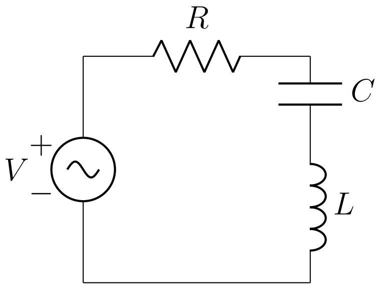

Figure 8. The series RLC resonator circuit.

The input impedance of a series RLC resonator is given by the equation

$$Z_{in} = R + j\omega L - j\frac{1}{\omega C} \tag{22}$$

where R is the resistance, L the inductance and C the capacitance of the circuit. The angular frequency ω relates to frequency f by $\omega = 2\pi f$.

Resonance occurs when at a particular frequency ω_0, the capacitive reactance of the capacitor and the reactive inductance of the inductor are equal, cancelling each other out and resulting in the total impedance of the circuit being at its minimum (Fig. 9). Solving this gives us the resonant frequency of the circuit:

$$\omega_0 = \frac{1}{\sqrt{LC}} \tag{23}$$

The (resistive) losses in the RLC circuit will cause damping of the harmonic oscillator, causing energy to be dissipated and the oscillation amplitude to decrease over time. This energy dissipation is described by the quality factor of the oscillator Q

$$Q = \frac{\omega E_{stored}}{P_{loss}} \tag{24}$$

where E_{stored} is the average energy stored in the resonator and P_{loss} the power dissipated due to the losses in the resonator.

The quality factor also defines the bandwidth of the resonator:

$$Q = \frac{\omega_0}{\Delta\omega} \tag{25}$$

where $\Delta\omega$ the full width at half maximum bandwidth of the resonator (the width of the frequency range where more than half of the power of the incoming signal is attenuated when compared to the resonance minimum).

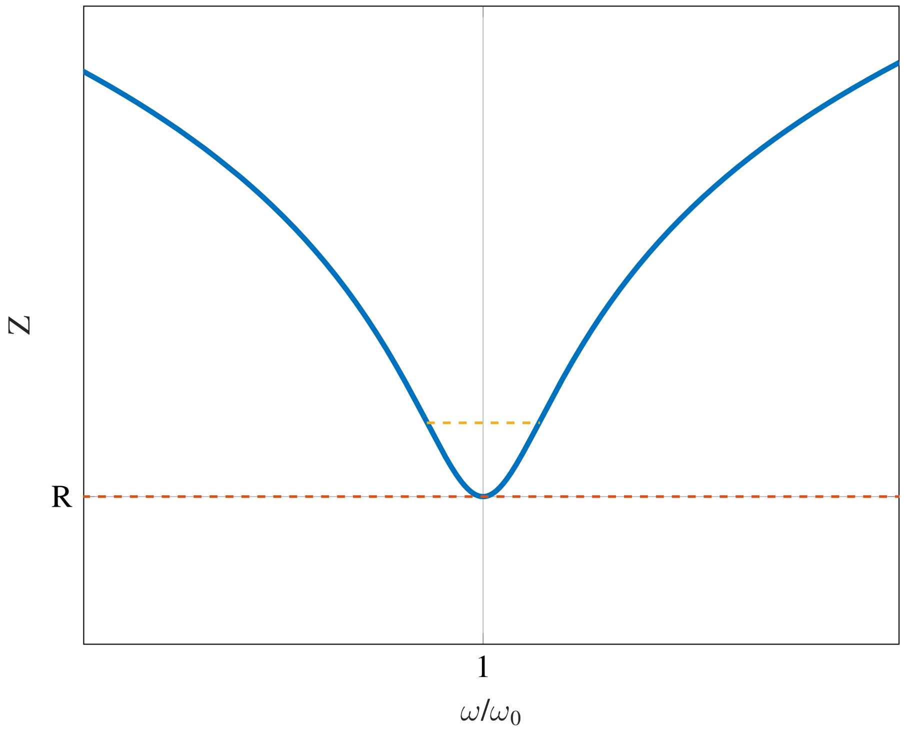

Figure 9. The impedance of a series RLC resonator. The yellow line depicts the bandwidth of the resonator at the -3 dB power point of $Z = R/0.707$. The minimum impedance of the resonator is defined by the resistance R, depicted with the red line.

The average energy stored in the inductor and capacitor are defined as

$$E_m = \frac{1}{4}|I|^2 L \tag{26}$$

and

$$E_e = \frac{1}{4}|V_C|^2 C = \frac{1}{4}|I|^2 \frac{1}{\omega^2 C} \tag{27}$$

where I is the current in the resonator.

At resonance, energy stored within the capacitor and the inductor are equal: $E_{stored} = E_e + E_m = 2E_e$. Losses in the ideal RLC resonator are purely resistive, so $P_{loss} = |I|R/2 = |V_C|/2R$. Therefore, by combining Eqs. (24), (26) and (27), the intrinsic (unloaded) quality factor of the RLC resonator is

$$Q_i = \frac{\omega_0 L}{R} = \frac{1}{\omega_0 RC} \tag{28}$$

Q_i is dependent on the properties of the components in the resonator and possible losses in the materials of a physical RLC resonator.

When the resonator is coupled to a load, such as a transmission line (associated with an impedance Z_0, where the transmission line is terminated at both ends with the impedance Z_0), the system has an associated loss which can be accordingly characterized by a quality factor Q_c, the so-called coupling quality factor. If coupled via a coupling capacitor with the capacitance of C_c, energy from the RLC resonator radiates to the transmission line at the rate of [30]

$$P_{loss} = \frac{1}{2}|I_{loss}|^2 R = \frac{1}{4}|V_C|^2 \omega_0^2 Z_0 \tag{29}$$

where $I_{loss} = |V_C| Z_{C_c}$, and $R = Z_0/2$. Therefore, the coupling quality factor is given as [30]

$$Q_c \approx \frac{2(C + C_c)}{\omega_0 Z_0 C_c^2} \tag{30}$$

The overall quality factor of the RLC resonator system is defined as

$$\frac{1}{Q_{tot}} = \frac{1}{Q_c} + \frac{1}{Q_i} \tag{31}$$

This is the total quality factor of the resonator as measured by an instrument coupled to the transmission line.

4.2 The transmission of the RLC resonator

In RF engineering, the output of a device is typically characterized using scattering parameters (S-parameters), which are simply the ratio of the voltage signals measured between two ports on the device as a function of the signal frequency. For example, S_{21} characterizes the transmission from port 1 to 2. The S-parameters are a complex quantity, as an AC signal passing through a device can experience phase shift in addition to attenuation. The scattering parameters of a device can be measured using a vector network analyser (VNA).

The S_{21} of an RLC resonator can be calculated by considering an applied voltage to the input port (port 1) of a network with the impedance of the feed line Z_0, which is typically 50 Ω.

$$S_{21}(\omega) = \frac{2}{2 + Z_0/Z_{in}} \tag{32}$$

The ratio Z_0/Z_{in} is given as [37]

$$\frac{Z_0}{Z_{in}} = \frac{2Q_i}{Q_c}\frac{1}{1 + 2Q_i x_r} \tag{33}$$

where $x_r = (\omega - \omega_0)/\omega_0$ is the fractional frequency shift.

By combining Eqs. (31), (32) and (33), a model for the total S_{21} for the RLC resonator can be determined:

$$S_{21} = 1 - \frac{Q_{tot}}{Q_c}\frac{1}{1 + 2jQ_{tot}x_r} \tag{34}$$

This results in the resonator exhibiting the Lorentzian line shape centred around ω_0 with a full width at half maximum bandwidth of ω_0/Q_{tot}, demonstrated in Fig. 10.

By measuring the S_{21} of a resonator, it is possible to extract the quality factors. The quality factor is a critical aspect in determining the performance of the resonator in applications, as it can describe the losses present in the material and the bandwidth of the resonator itself, which in turn determines the amount of individually addressable resonators that can be coupled to a single transmission line.

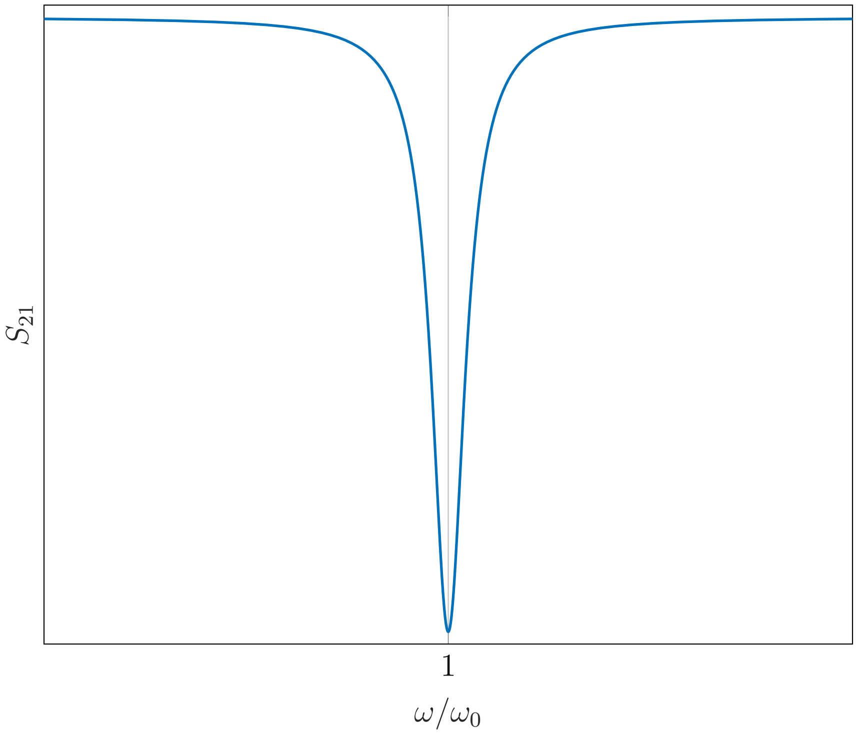

Figure 10. The S_{21} of a resonator as described in the model in Eq. (34).

5 KINETIC INDUCTANCE BOLOMETER

As discussed in section 2.2.1, the kinetic inductance phenomenon can be used for very sensitive radiation detection in the KID. Although operating in a very similar fashion, the KIB offers many advantages when compared to the KID, such as not requiring sub-Kelvin temperatures to operate and not requiring cryogenic or SQUID preamplification. In this chapter, I introduce the operating principles of the KIB.

5.1 Fundamentals of the bolometer

The bolometer is one of the oldest methods for radiation detection. Invented in 1878 by the American astronomer Samuel Pierpot Langley [38] for measuring the infrared radiation of celestial objects, the bolometer turned out to be a very flexible technology for a variety of different radiation detection tasks from single photon detection for quantum computer readout circuitry [39] to large scale radio astronomy.

The bolometer measures the power of incident electromagnetic radiation by the temperature change caused when the radiation is absorbed in a material. A basic bolometer consists of an absorptive element and thermal volume with heat capacitance C connected to a thermal bath at a temperature of T_b through a thermal conductance G. The radiation absorbed by the bolometer increases the temperature T of the device, dependent on the incident power P_{inc} (Fig. 11).

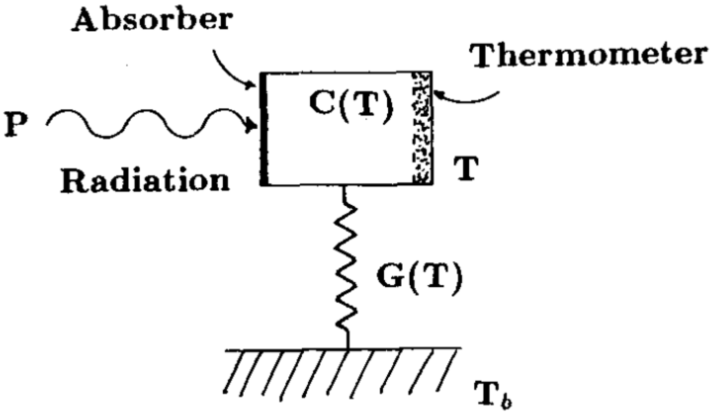

Figure 11. Thermal equivalent circuit of a bolometer [21].

The thermal balance equation describes the time dependent behaviour of the bolometer [40]:

$$C\frac{dT}{dt} + G(T - T_b) = P_{inc} \tag{35}$$

The thermal time constant τ_{th} associated with the device is defined by the ratio of the heat capacitance of the absorber to the thermal conductance between the device and the thermal reservoir.

$$\tau_{th} = \frac{C}{G} \tag{36}$$

The thermal time constant sets the fundamental thermal bandwidth of the bolometer, as defined by the thermal cut-off frequency

$$f_c = \frac{1}{2\pi\tau_{th}} = \frac{G}{2\pi C} \tag{37}$$

The bolometer possesses many desirable characteristics as a radiation detector, as it is by nature sensitive to a broad band of electromagnetic radiation. As the radiation is absorbed in the bolometer and the energy converted to heat, there are no fundamental limits to the wavelengths detectable by the bolometer. Due to the time constant associated with the thermal equivalent circuit, the bolometer is self integrating. This means that the bolometer effectively averages the power of the incoming radiation over the thermal time constant. High sensitivities through low thermal capacities and conductivities are simple to achieve with modern microfabrication techniques and their construction does not rely on any exotic materials and can be made to be fully compatible with standard complementary metal oxide semiconductor (CMOS) processes.

For a maximally sensitive bolometer, the heat capacity C should be as low as possible. Therefore, in practical applications, the value of C and G is optimized to achieve as high a sensitivity as possible while maintaining a time constant short enough for a fast responding sensor.

Fabrication of the most sensitive bolometer relies on maximizing the optical coupling of the radiation to the absorptive element, which can be achieved for example by increasing its optical size. Thermal mass and conductance can be tuned to achieve a desired thermal operating point, sensitivity, noise and responsivity, depending on the properties of the thermal transducer and the signal amplifying electronics.

To achieve wide bandwidths and high sensitivities, the bolometer has to be optimized according to Eqs. (37) and (38). Fabricating such features can be achieved using micromachining techniques from semiconductor manufacturing processes. For example, a large surface area nanomembrane only coupled to the thermal bath through thin suspension legs can be fabricated on a silicon wafer substrate using thin film deposition and patterning via stereolithography and anisotropic plasma etching.

5.2 Superconducting bolometers

Bolometers utilizing conventional electronics at room temperatures suffer from several drawbacks. Typically, the response times of such detectors are slow. Dissipation of energy in the bolometer due to resistive losses in the thermal transducer (self-heating) can also cause stability issues at room temperature. For example, if the temperature coefficient of the losses is high enough, the dissipated power can quickly run away if the temperature of the bolometer rises too high, effectively causing sensor latch-up. Noise emanating mostly from the thermal fluctuations in the temperature transducer itself (phonon noise) and the Johnson noise in the resistive components of the whole bolometer circuit limit the available resolution and sensitivity of the sensor significantly.

The phonon noise equivalent power (NEP) is given by the equation [41]

$$NEP = 4k_BT^2G \tag{38}$$

Johnson noise is generated by the thermal fluctuations of the charge carriers inside an electrical conductor. Johnson voltage noise in a resistor at temperature T is given as [41]

$$v_n = \sqrt{4k_BTR\Delta f} \tag{39}$$

where R is the resistance and Δf the bandwidth.

Using cryogenic bolometers bypasses many of the shortcomings of the room temperature bolometer, such as significantly reducing both the phonon and Johnson noise. Cryogenic bolometers can reach a NEP several orders of magnitude lower than their room temperature counterparts. The low temperatures also allow taking advantage of superconducting materials with extremely low losses to minimize the self-heating effect, as well as the exploitation of the superconducting phenomena such as the kinetic inductance.

5.2.1 Kinetic inductance as a thermal transducer

The kinetic inductance phenomenon can be exploited as an extremely sensitive temperature sensor. The first KIB, introduced by Sauvageau and McDonald in 1989 [21], utilized the temperature dependent kinetic inductance of a thin film of niobium as the thermal transducer of a bolometer. Due to the small dimensions of the film, the total impedance of the film is dominated by the kinetic inductance at the bolometers operating temperature. As the device operates below the superconductor critical temperature, it has no intrinsic Johnson noise, and it can accommodate very large sensing currents without self-heating. Ideally, the performance of the KIB is dominated by phonon noise, as described in Eq. (38). Theoretical analysis indicated that due to the high sensitivity of the kinetic inductance to temperature fluctuations, NEP of the order 10^{-20} W is achievable in an ideal device.

The temperature dependency of kinetic inductance is due to the population of supercurrent carrying Cooper pairs decreasing as the temperature increases. The presence of quasiparticles and the finite inertia of the Cooper pairs result in the complex conductivity, as described by the Mattis-Bardeen theory in section 3.3.

High initial kinetic inductance of superconducting films can be obtained by utilizing highly disordered materials. The kinetic inductance at 0 Kelvin $L_{kin}(0)$ can also be estimated with [25]

$$L_{kin}(0) = \frac{\hbar R_{ns}}{\pi \Delta(0)} \tag{40}$$

where R_{ns} is the normal state sheet resistance of the structure.

According to Eq. (40), the initial kinetic inductance can be maximized by using a material with a high normal state resistivity. Niobium nitride (NbN) has been recognized as one such material.

The kinetic inductance at absolute zero is described in terms of Cooper pairs by Eq. (21). As the penetration depth has a dependency on temperature by Eq. (13), the temperature dependence of the kinetic inductance as described by the two-fluid model by combining these two equations is given as

$$L(T) = L_{kin}(0)\left[1 - \left(\frac{T}{T_c}\right)^4\right]^{-1} + L_g \tag{41}$$

The expression for the kinetic inductance can be generalized to the form

$$L_{kin} = L_{kin}(0)\left(\frac{\lambda}{\lambda_0}\right)^2 \tag{42}$$

Similarly, the penetration depth as described by the Mattis-Bardeen theory in Eq. (17) gives Eq. (42) a dependency on temperature.

Small perturbations in the inductance of a superconducting circuit can be precisely measured by using the resonant RLC circuit, as described in chapter 4.

6 THZ IMAGING SYSTEM

VTT has been developing superconducting sub-millimeter wave detectors and relevant hardware for over 20 years [42–49]. The latest developments have concentrated on the KIB technology with the goal of scaling up to a large-scale sensor array to be utilized in terrestrial imaging systems. This has resulted in the passive terahertz video camera called LASTKID (Large area staring kinetic inductance focal plane arrays operating at elevated temperature). LASTKID offers many novel advantages for terahertz technology in the security imaging application. The passive nature of the system allows the system to be used as a video camera with no need for expensive coherent terahertz sources. The large array of detectors eliminates the need for optomechanical scanning and therefore increases sensitivity, as longer integration time per pixel is possible while maintaining video frame rates. The architecture of the resonant readout scheme of the bolometers allows for scalable RF multiplexing, with over a hundred bolometer pixels on a single RF transmission line and readout electronics. The electronics are based on standard, widely available RF components which operate outside the cryostat at room temperature. The imaging system operates with a closed-cycle Gifford-McMahon cryocooler in the range of 4 to 10 Kelvin [50].

The LASTKID (Fig. 12) comprises a focal plane array of superconducting kinetic inductance bolometers inside a cryostat and a quasi-optical system consisting of windows to the cryostat, lenses, filters, and reflectors. The readout electronics and data acquisition are placed outside the cryostat at room temperature, with RF transmission line feedthroughs to the cryostat.

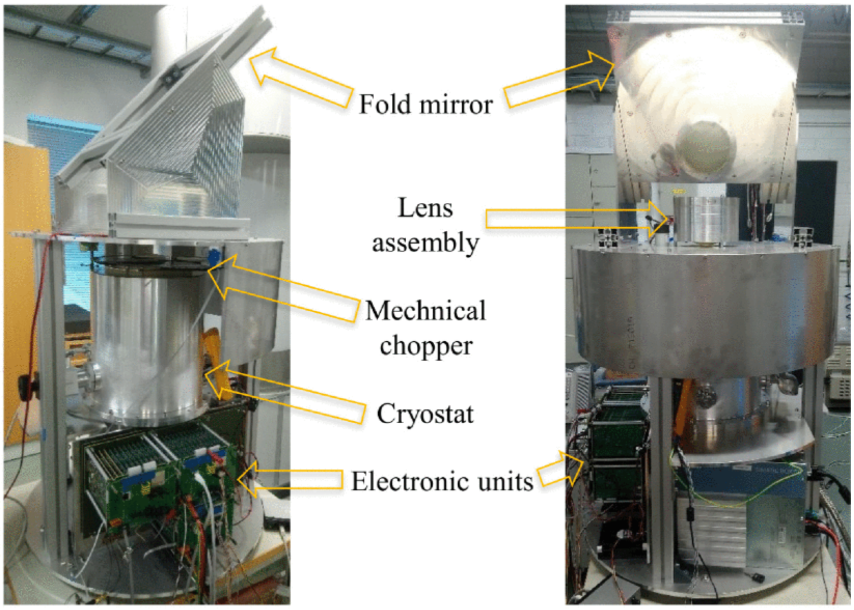

Figure 12. The LASTKID imaging system [51].

The total height of the instrument is about 130 cm, with a footprint diameter of 65 cm. The total system weight is 80 kg, excluding the cryocooler compressor. The closed-cycle cryocooler has a base temperature down to 4.8 K.

The imaging specifications of LASTKID have all been designed with the final safety imaging application in mind. The detection band (Fig. 13) is the sub-millimeter wave band from 0.2 to 1 THz, which is defined as a compromise between the spatial resolution, as defined by the wavelength-dependent diffraction limit, and penetration through the dielectric materials of standard items of clothing [15].

Similarly, the radiometric sensitivity and dynamic range for the detectors are set by the application. The noise equivalent temperature difference (NETD), i.e., the smallest temperature difference detectable by the imaging system, needs to be lower than 100 mK to be effective in standoff detection of concealed items [52]. On the optics side, the wide field of view and high magnification required for imaging human-sized objects at close range sets the system parameters for the optical system, which set restrictions to the design parameters for the focal plane detectors.

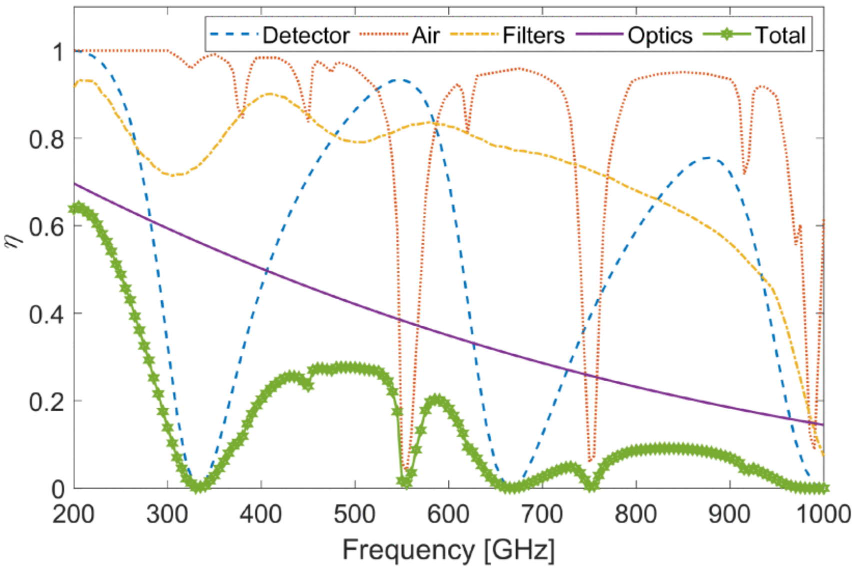

Figure 13. The total optical efficiency of the LASTKID optical system [51].

6.1 Focal plane bolometer array

The focal plane array (FPA) consists of three detector tiles (Fig. 14) with 8712 bolometer detectors in total, which have been divided into 66 readout channels. Each detector tile is fabricated on a single 150 mm silicon wafer, by utilizing multiple thin film deposition and patterning processes at the Micronova cleanroom facilities in Otaniemi, Espoo. Starting with a silicon on insulator (SOI) wafer, metal layers are reactively sputtered using OEM Mark IV inductively coupled plasma sputtering system. The layers are patterned using stereolithography with a Canon FPA3000-i4 and reactive ion etched with LAM Research dry etchers.

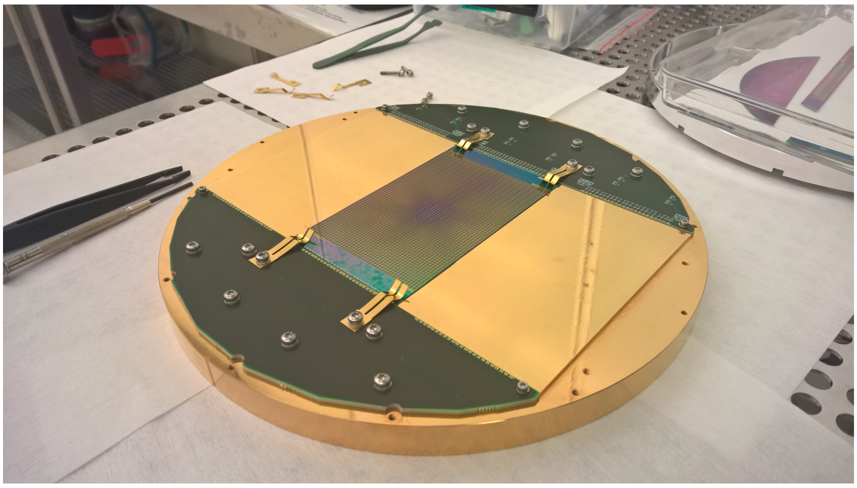

Figure 14. One of three focal plane array tiles arranged on the cold plate.

Each bolometer sensor element consists of a 200 nm thick membrane of silicon nitride (SiN) with a 90 nm thick niobium nitride (NbN) superconducting meander, whose temperature dependent kinetic inductance acts as the temperature transducer. The temperature change of the nanomembrane is caused by the terahertz radiation power dissipated in a 100 nm thick resistive titanium tungsten (TiW) grid absorber, which is collocated with the kinetic inductance thermometer on the nanomembrane (Fig. 15).

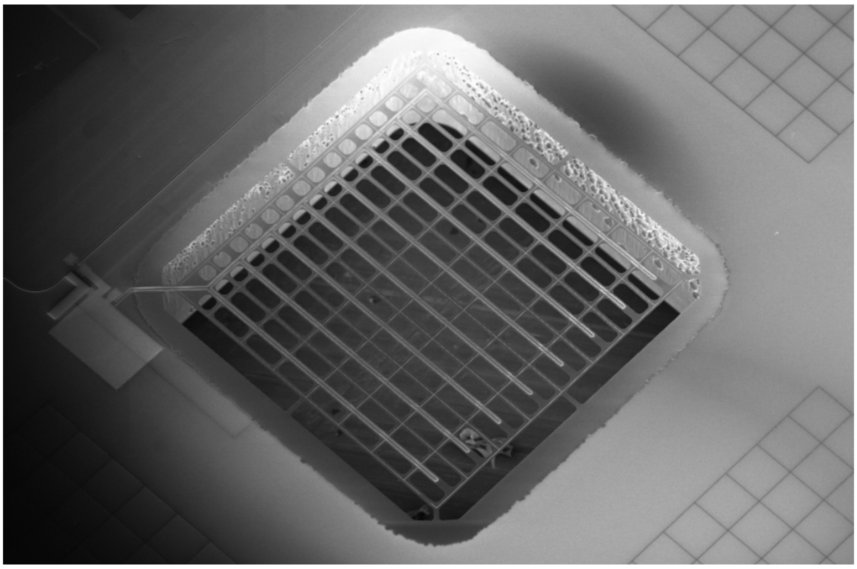

Figure 15. An electron microscope image of a single KIB membrane.

The very thin and high room temperature resistivity NbN film means that the total inductance of the superconducting meander is dominated by the kinetic inductance L_{kin}. The high kinetic inductance fraction ($\alpha_{kin} = L_{kin}/(L_g + L_{kin})$) gives the detector a large responsivity to thermal fluctuations [20]. The temperature-sensitive total inductance $L(T)$ together with a parallel connected shunt capacitor C_s form a lumped element LC resonator. Each resonator in a readout channel is connected to a common superconducting transmission line through a series coupling capacitor C_c, which matches the impedance of the resonator to the transmission line for the radio frequency readout (Fig. 16).

The temperature-dependent resonant frequency f_r of each LC resonator is given by the equation

$$f_r = \frac{1}{2\pi\sqrt{L(T)(C_s + C_c)}} \tag{43}$$

The resonant frequencies of the RLC resonators are in the order of a couple of hundred

MHz. The chosen frequency band of 20 to 300 MHz for the detectors is the result of compromising two factors. As observed in previous work, the resonator quality factor decreases as a function of frequency [44], being small at the high frequency bound while the electrical response time of the resonator becomes too slow for multiplexing at low frequencies. By virtue of the high detector responsivity, the modulation of the resonance frequencies due to the change in the bolometer temperature is high enough to be detected with inexpensive room temperature electronics, eliminating the need for cryogenic amplification or high bandwidth low noise amplifiers (LNA).

The design parameters of the KIB circuit are presented in Table 1. The total inductance of the resonator is formed by the geometric inductance L_g and the kinetic inductance L_{kin} of the superconducting meander. In the case of LASTKID, the inductance is kept constant across all resonators and the value of the shunt and coupling capacitors are varied to tune each resonator native frequency. The capacitors are realized on the wafer as parallel plate capacitors. To decrease the size of the capacitors and therefore increase the density of sensor elements on the wafer, atomic layer deposition (ALD) aluminium oxide (AlOx) with the high relative permittivity of approximately 9 is used as the capacitor dielectric.

Table 1. The design values of the resonator capacitances and inductances and their respective resonant frequencies.

C_s	C_c	L_g	L_{kin}	f_r
4 - 300 pF	1 - 18 pF	7 nH	~100 nH	25 - 300 MHz

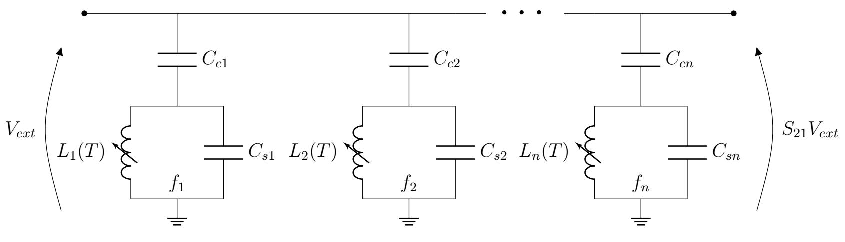

Figure 16. KIB resonator array equivalent circuit, from the first to the nth resonator in a single readout channel.

The nature of the lumped element LC resonator allows each bolometer to be tuned to a specific frequency in the spectrum, with each sensor individually probed with a readout tone at the resonant frequency [53]. When the readout tone V_{ext} is applied to the resonator array, the tone is modulated by the bolometer signal, resulting in the output voltage of $S_{21}V_{ext}$, where S_{21} is the transmission through the resonator array.

Optical radiation coupling to the absorber is achieved by matching the sheet resistance of the grid absorber to the vacuum impedance of 377 Ω. The coupling of the radiation is further increased with a reflective back cavity behind the membrane. In LASTKID, the metallic cold finger acts as the backshort with the height of the cavity defined by the thickness of the silicon substrate of the detector array itself. The reflector causes constructive interference on the detector membrane at the wavelengths of $h_{bs} = n\lambda/4$, where h_{bs} is the height of the cavity (450 µm), n is an odd integer and λ the wavelength of the radiation.

The response time and sensitivity of the bolometer are determined by its thermal mass and conductance to the thermal bath. Measured parameters of the previous generation KIB according to [43] are listed in Table 2.

Table 2. Thermal capacity and conductance of a similar KIB to the one under study in this thesis.

C	G
120 pJ/K	18.2 nW/K

The parameters implicate a thermal time constant τ_{th} of approximately 6 ms and thermal cut-off frequency f_c of the order of 24 Hz.

The noise performance of the KIB is limited by phonon noise, as given by Eq. (38). In [51], the total NEP of the system was estimated to be 14 fW/Hz$^{1/2}$. This is estimated to correspond to a NETD of 10 mK/Hz$^{1/2}$, easily surpassing the requirements for standoff security detection. The responsivity of the detector $\mathfrak{R}$, i.e., the voltage signal per incident radiation power, define the noise temperature of the detector and therefore define the design parameters for the readout electronics and amplification. Assuming operation at resonance frequency and $Q_i \gg Q_e$, the responsivity as depicted in Eq. (44) depends on the thermal conductance of the bolometer G, normalized nonlinearity of the bolometer inductance $L^{-1}(dL/dT)$, the resonator intrinsic quality factor Q_i and the system impedance Z_0 [53].

$$\mathfrak{R} = \sqrt{(\alpha/G)L^{-1}(dL/dT)Z_0Q_i} \tag{44}$$

Here, the parameter α is related to the excitation power and the onset of the Duffing mode. Too high of an excitation power causes resonator non-linearities due to bolometer self-heating and other parasitic phenomena [43], which distort the line shape of the resonator response into a Duffing-like response and drag the resonant frequency down. Stable operation of the detector requires α to be less than 0.8. Further details of resonator non-linearities can be found in [54].

Based on previous work, the responsivity of LASTKID is estimated to be in the range 0.8 - $1.8 \cdot 10^5$ V/W.

6.2 Quasi-optical system

Terahertz radiation is able to enter the cryostat through an optical window on the top of the LASTKID cryostat. The quasi-optical system is used to shape and focus the incoming thermal terahertz radiation on the focal plane array of bolometers (Fig. 17). The driving specifications for the design of the optical system for use in concealed item detection is the adequate filtering of thermal infrared radiation, relatively wide field of view (FOV) at short ranges, minimizing the optical losses and achieving sufficient optical resolution with the relatively small detector size.

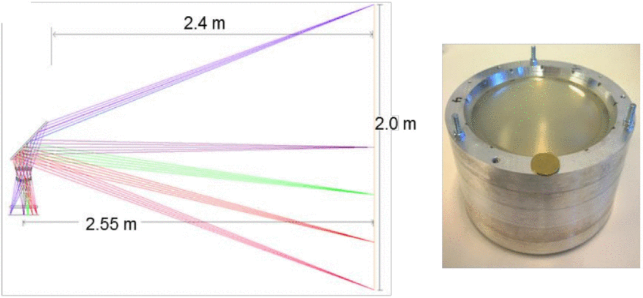

(a) (b)

Figure 17. (a): Ray tracing image of the optical system, with the imaging plane on the right. (b): The lens assembly. [51]

The design of the optical system is ultimately governed by fundamental trade-offs in the system parameters, such as the FOV, imaging distance, depth of field (DOF) and maximum spatial resolution Δx as limited by diffraction. Additionally, these parameters provide input for determining factors such as the focal plane area and the number of detectors, which in turn determine the electronic and cryogenic requirements.

Although lens-based optics for THz suffer from rather high transmission losses, a compact optical system with a sufficiently low f-number is best achieved with a low-loss polymer lens-based arrangement. Compared to an arrangement based on silicon lenses, polymer lenses are more cost-effective to manufacture and have lower reflection losses due to their lower index of refraction. A reflector based optical system could also be utilized, but the much greater size and the increased complexity of the reflector arrangement would outweigh the benefits. The lenses in the LASTKID system are realized with TPX polymer (trade name for polymethylpentene manufactured by Mitsui Chemicals), which has high transparency and a refractive index of approximately 1.46 at the frequency range of interest [55].

Filtering of thermal infrared, which would otherwise prevent the cryostat from cooling down and dominate the bolometer thermal signal, is realized by combining metal mesh thermal filters such as those described in [56] and Zitex polymer filters [57]. These filters define the upper cut-off frequency of the optics at 1 THz.

The optics of LASTKID have been characterized in [50]. The measurement of the point spread function (PSF) for the optics verifies the near-diffraction-limited optical resolution of 17 mm on the imaging plane, meeting the requirement for concealed item detection.

6.3 Readout electronics and data acquisition

The readout electronics (Fig. 18) utilize a dispersive transmission measurement scheme, where the amplitude and phase of a readout tone pass through the bolometer array transmission line, after which this is detected and compared to the original tone (Fig. 19). An RF transmission line to the detector tiles is achieved through vacuum a feedthrough in the cryostat, also containing RF attenuators to thermalize the readout signals. A full review of the readout electronics can be found in [53].

The distinct, easily tunable resonant frequency of the bolometers enable a simple TDM scheme. During a frame time τ_F, each detector in a channel is addressed sequentially in a time slot of $\tau_s = \tau_F/N$ with a corresponding resonance frequency f_{ri}. Here N is the number of resonators in the readout channel. This serial addressed frequency excitation (SAFE) is possible due to the relatively slow thermal time constant of the sensors. Typically, similar multiplexed systems use a frequency comb readout tone, which requires high bandwidth from the digital and analog circuitry. In SAFE, the carrier tone gets modulated by the incoming THz radiation signal. The modulated signal is amplified at room temperature (with the amplifier noise temperature T_N = 35 K) and demodulated to the baseband frequency, resulting in time-multiplexed detector signals, recorded on an external PC for post-processing. In this approach, no other high-speed digital electronics besides a sim-

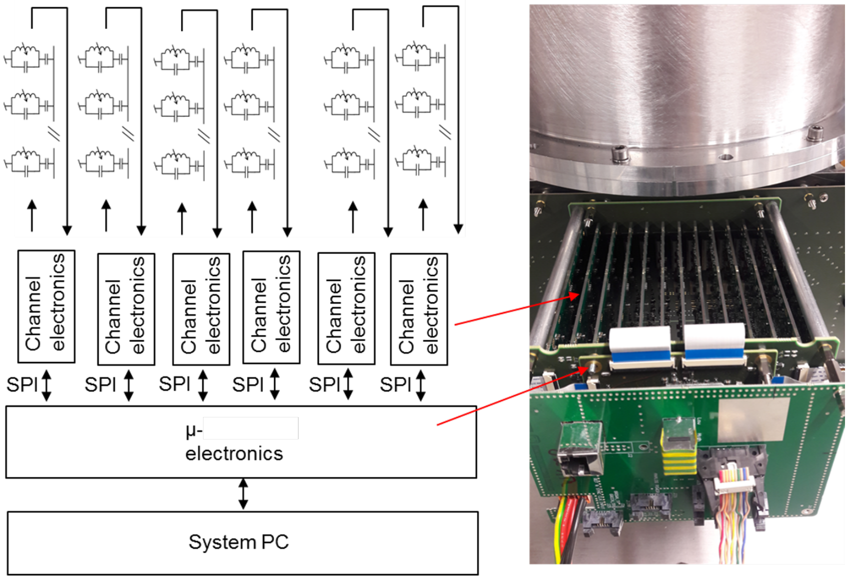

Figure 18. The readout electronic assembly on the side of the cryostat [53].

ple RF synthesizer with a sinusoidal output and an analog-to-digital-converter (ADC) are needed. The digital signal processing requirements are essentially reduced down to the digital sampling rate of f_S, instead of the full readout band.

The benefit of SAFE is that high-speed digital electronics are only needed to generate the sinusoidal excitation tones. This makes the readout system drastically less expensive as compared to a full frequency division multiplexing topology. In the ideal case of the phonon noise being the dominant noise mechanism, multiplexing does not decrease the signal-to-noise ratio (SNR), as compared to the continuous readout of a single detector.

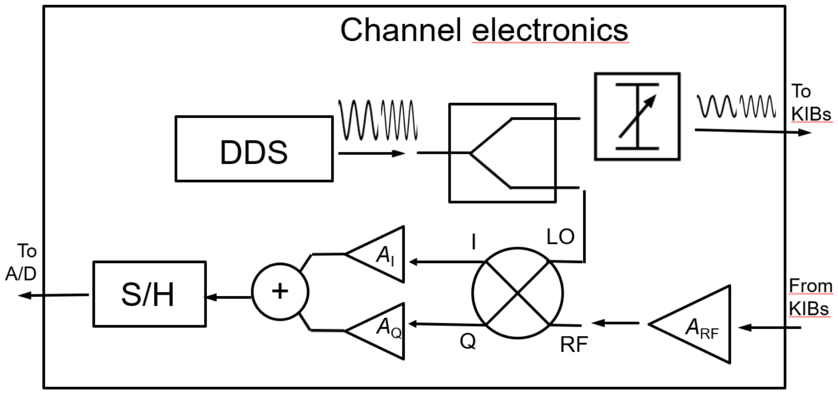

Figure 19. Block diagram of the readout electronics of a single channel [53].

An optomechanical chopper is used to induce modulation to the optical signal, filtering the effect of temperature oscillations of the cold head and the other low-frequency noise and bias drift.

6.4 Imaging in practise

For practical readout of signals in an imaging setting, finding the correct parameters for the RF excitation signals is required, in particular the frequency and the phase reference for each detector and the whole transmission line. To find the optimal frequency-dependent phase reference, first, the excitation frequency is swept through the readout band. The transmission has a sinusoidal envelope due to the propagation delay of the excitation signal through the transmission line, depicted in Fig. 20 (a). To fix the reference to a constant value at all frequencies, the phase reference is calibrated to compensate for the delay using the phase and frequency offset values obtained by fitting a sinusoidal curve to the envelope. The excitation power level is chosen to maximize the responsivity while avoiding the onset of the nonlinear resonance mode. In the case of LASTKID, the absolute value of the excitation is approximately 20 nW, referenced to the input of the readout channel. The transmission measurement is repeated with the corrected variable phase reference, and the result is plotted in Fig. 20 (b). As the responsivities of the detectors are proportional to the steepness of the slope of the voltage output signal, the corresponding responsivity spectrum as the frequency derivative of the transmission data is plotted in Fig. 20 (c) and the peak values picked as the frequency calibration points f_{ri}. As can be seen from the responsivity plot, the absolute responsivities of the detectors vary throughout the readout channel due to the variations in the detector quality factors and the slight variations of their RF matching conditions to the transmission line.

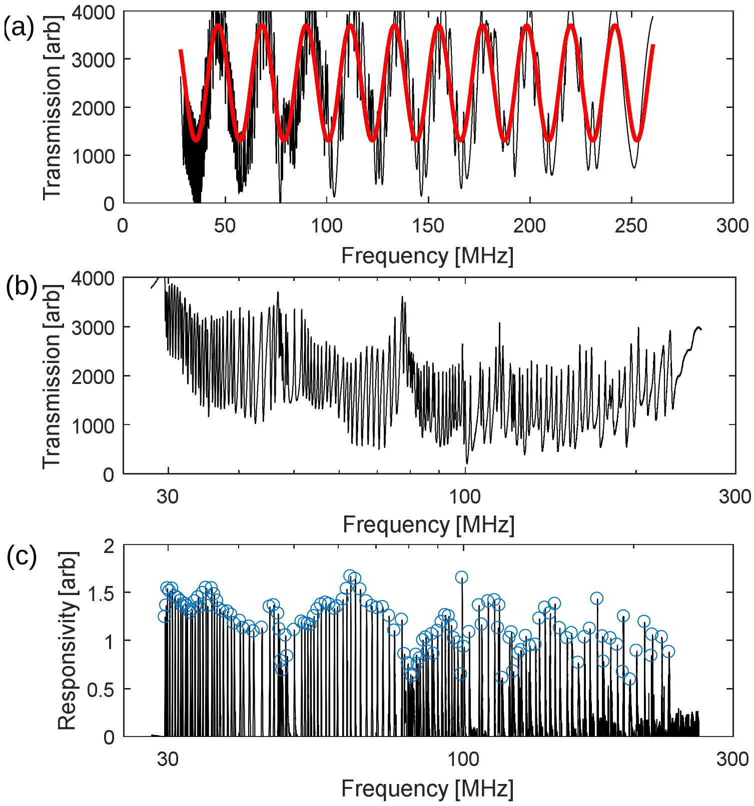

Figure 20. The transmission data from the readout electronics and the readout calibration [53].

For recording the video images, the data is recorded from the readout electronics onto an external PC in the time domain. To produce a legible image, post-processing procedures take place. First, the data is demultiplexed and demodulated to the baseband using the frequency of the optomechanical chopper as the local oscillator. The data is then averaged to the final video frame rate of 9 Hz and the signal offset subtracted. The cold stage of the cryostat recycles helium gas in cycles of 1 Hz, creating thermal interference to the signal at this frequency and its harmonics, which needs to be removed. Also, discrete errors to the X-coordinates of pixels are introduced as the resonant frequencies and the detector indices do not match up. To calibrate the X-coordinates, a plastic pipe filled with hot water is utilized. The vertically aligned pipe is slowly moved horizontally in the imaging plane with an XY-manipulator, providing a reference signal for spatial calibration. To further calibrate for the varying bolometer responsivities, a copper plate is placed on top of the lens system to provide reference data. With the aid of this data, the pixels are spatially reorganized and corresponding detector signals normalized. Finally, the video is gamma-corrected to set the proper contrast and brightness for the resulting video.

The product of this procedure is a video at the frame rate of 9 Hz. Example images can be seen in section 7.4, resulting from the measurements conducted as a part of this thesis.

7 EXPERIMENTS

The experimental part of this thesis consists of three distinct measurements and an imaging experiment.

First, measurements of the resistivity and the critical temperature of the superconducting NbN films were performed. The measurements utilized test structure samples from the same wafer as is installed in LASTKID focal plane array. The goal of these measurements was to determine the values of the critical temperature T_c, the gap energy $\Delta(0)$ and the penetration depth $\lambda(0)$ from the samples. This data was utilized both in verifying process parameters and in the data analysis of the second measurement.

In the second measurement, the RF transmission characteristics were measured from several LASTKID readout channels over a temperature sweep from 4.5 to 9 Kelvin, to determine the characteristics of the KIB resonators. The measured S_{21} parameters were then fitted with a resonator model to obtain the characteristic frequency and quality factors of each individual resonator. The resonance frequency was used together with the shunt capacitor design parameters to determine the kinetic inductance of each resonator. The kinetic inductance and intrinsic quality factor of the resonators were then analysed in the context of the two-fluid and the Mattis-Bardeen model.

In the third measurement, an aqueous blackbody terahertz source was used to characterize the noise characteristics and the thermal cut-off frequency of the KIBs. An optical chopper placed in between the blackbody source and the imaging system provided the reference signal. The KIB response was then captured using the LASTKID readout electronics. The obtained time-domain signal was analysed using Fourier transform to determine the frequency response of the KIBs.

In the imaging experiment, all available electronics channels are calibrated to record video images on a portion of the focal plane array. The data from the experiment is used to demonstrate the imaging capability of the system and to verify its performance in concealed item detection application.

7.1 Niobium nitride thin film characterization

To obtain data on the critical temperature T_c and the resistivity of the niobium nitride thin films, measurements were conducted in a dedicated measurement setup outside the imaging system (Fig. 22). The samples were obtained from test structures fabricated on the same wafers as the full bolometer arrays in the imaging system, where the thickness of the Sup1 layer is 90 nm and Sup2 150 nm.

The samples were as listed in Table 3.

Table 3. Samples from wafer LK6.

Chip	Mask Layer	Structure
2	Sup1	Van der Pauw (100 x 100 µm^2)
3	Sup1	Van der Pauw (100 x 100 µm^2)
3	Sup2	Van der Pauw (100 x 100 µm^2)
4	Sup1	Van der Pauw (100 x 100 µm^2)

The samples were cleaved into separate chips, placed on a copper sample holder (Fig. 21), and then wire-bonded to the breakout circuit board. The sample holder and breakout PCB were mounted to the cold finger of an Optistat AC-V 75 cryostat and connected with copper and constantan twisted-pair looms for the DC measurements.

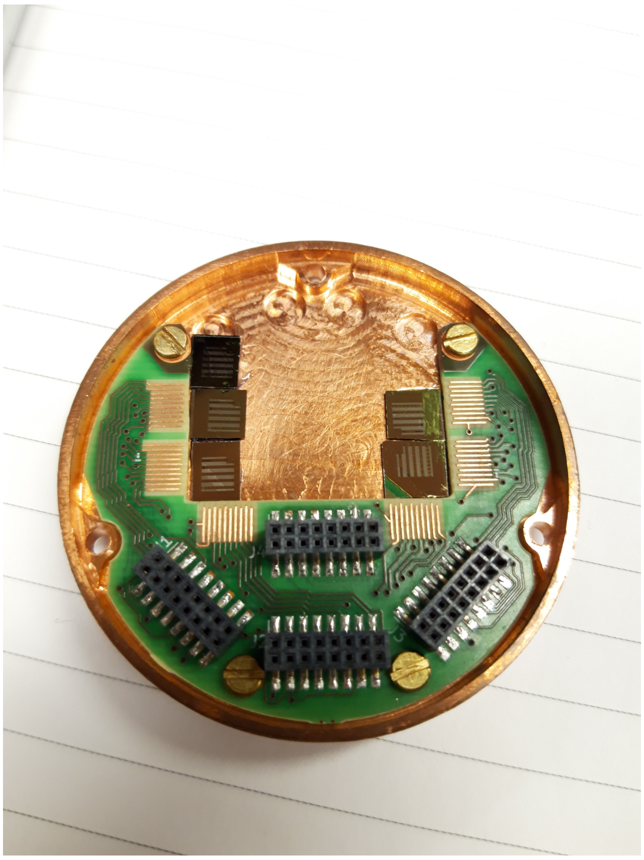

Figure 21. The sample holder with the thin film sample chips in place.

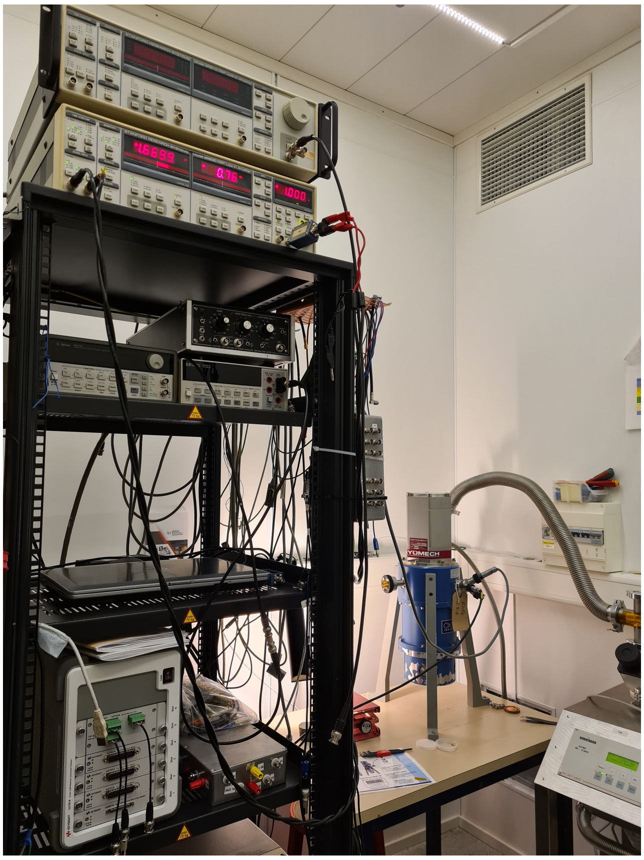

Figure 22. The T_c measurement setup.

The resistances of the samples were measured by using the four-wire sensing configuration with a Stanford Research Systems SR830 lock-in amplifier at a signal frequency of 13 Hz, with the bias current supplied through one twisted pair loom and the voltage measured through another. The bias current was generated using the reference voltage output of the lock-in amplifier with a load resistor in series with the sample. The bias current was determined by Ohm's law from the reference voltage and the load resistor. A 10 µA bias current was obtained with a 10 kΩ resistor and 0.1 V excitation voltage.

The temperature of the cryostat was controlled with an Oxford Instruments ITC temperature controller. For determining the rough T_c, the temperature of the cryostat was swept by hand and the drop of the measured resistance to zero was observed. Once the rough T_c was determined, a measurement script was used to slowly sweep the cryostat temperature first up and then back down to fully record the superconducting transition and the hysteresis.

7.1.1 Analysis

The measured temperature data is shown in Fig. 23 and the room temperature resistivities in Table 4, along with the calculated superconductor parameters. The oscillations visible in the measured temperature values are due to the discrete steps of the temperature sweep and the slight overshoot of the temperature controller as it settles to each new temperature point. One of the four terminals on sample Chip3Sup2 was open, so the measurement was completed in the two-wire configuration. Consequently, only the T_c data was available for this measurement.

Table 4. Wafer LK6 room temperature resistivities, critical temperatures and other calculated parameters.

Chip	Mask Layer	ρ_{RT}	T_c	$\Delta(0)$	$\lambda(0)$
2	Sup1	681.3 µΩcm	10.3 K	1.56 meV	850.9 nm
3	Sup1	611.7 µΩcm	10.5 K	1.59 meV	798.6 nm
3	Sup2	N/A	10.36 K	1.57 meV	N/A
4	Sup1	570.5 µΩcm	10.45 K	1.58 meV	773.0 nm

The T_c of each sample was determined by projecting the steepest slope of the transition to the 0 Ω line on both slopes of the hysteresis loop and taking their average.

Using the room temperature resistivity ρ_{RT} and the measured critical temperature T_c we

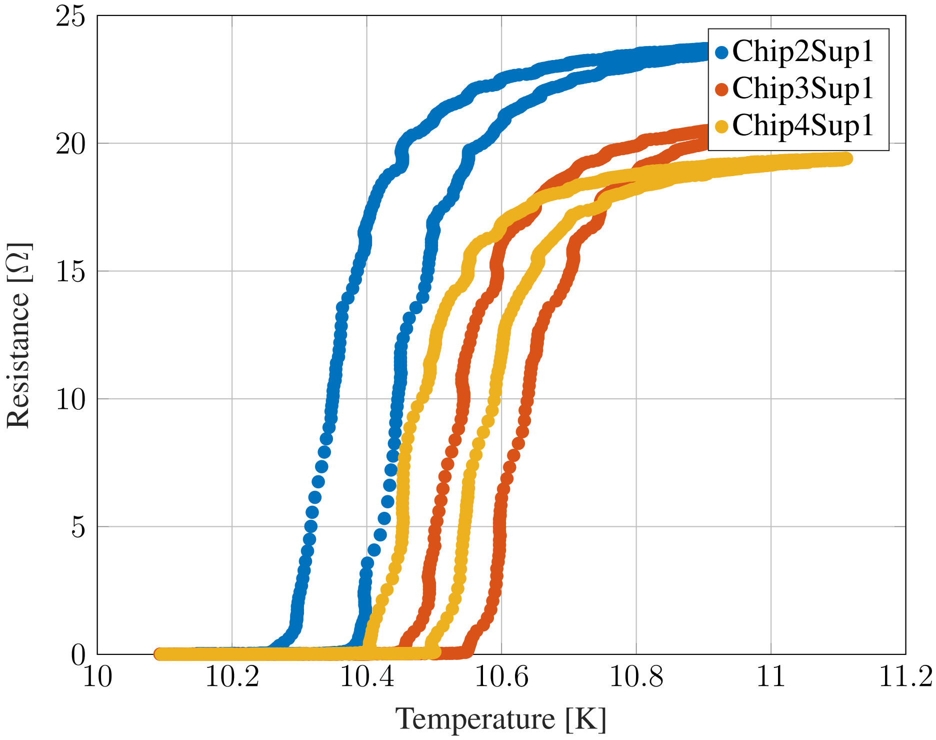

Figure 23. T_c measurement data.

can estimate zero-Kelvin energy gap $\Delta(0)$ and penetration depth $\lambda(0)$. The superconductor gap energy is estimated with the Eq. (16). From the obtained value of the gap energy and the measured room temperature resistivity of the sample, the penetration depth $\lambda(0)$ can be obtained with the equation

$$\lambda(0) = \sqrt{\frac{\hbar \rho_{RT}}{\pi \mu_0 \Delta(0)}} \tag{45}$$

7.2 RF transmission measurements of the bolometer array

To determine the resonant frequencies and the quality factors of the KIB resonators as a function of temperature, transmission data from several readout channels was measured as the thermal bath temperature of the cryostat cold finger was swept from 4.8 to 9 Kelvin.

The resonator array transmission characteristics were measured by an S-parameter S_{21} measurement in the complex format with a Keysight E8362B VNA. The VNA was connected in turn to each of the readout channels via a breakout printed circuit board (PCB) at the connector of the readout electronics, housing micro-miniature coaxial (MMCX) connectors for each channel. A Mini-Circuits ZX60-P103LN+ low noise amplifier (LNA) was included on the output line after the breakout PCB to boost the output signal level before the input of the VNA to well above the noise floor of the measurement. The measurement schematic is presented in Fig. 24.

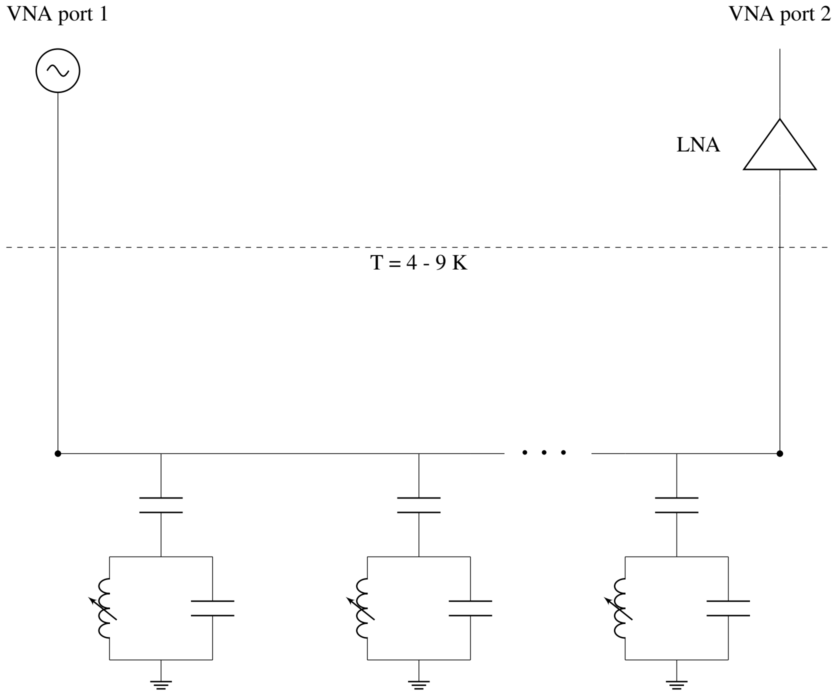

Figure 24. Schematic of the RF transmission measurement.

Excitation power of -32 dBm was used for all the measurements, to avoid resonator nonlinearities and the Duffing mode as described in section 6.1.

Due to the pulse tube of the cryocooler, the temperature of the cold head oscillates at the rate of 1 Hz. Despite closed-loop temperature control, a background oscillation of approximately 40 mK remains. To obtain the average effective bath temperature, a Hewlett Packard 34401A multimeter was used on the longest integration time setting to measure the voltage of the temperature sensor.

For the determination of kinetic inductance parameters of each bolometer, knowledge of the accurate resonant frequency is crucial. As a result, a high amount of 256 averages was used at each temperature point to suppress the variations caused by the temperature oscillations. The data destined for determining the quality factors was measured without averaging. Averaging would have lowered the measured quality factor due to the oscillation of the resonance frequency by broadening the resonator peak. The exact determination of each resonance frequency was not critical in the analysis of the quality factors.

The S_{21} spectra were measured in total from 10 readout channels on the central detector tile at 9 temperature points. An example of the measured averaged transmission data is presented in Fig. 25.

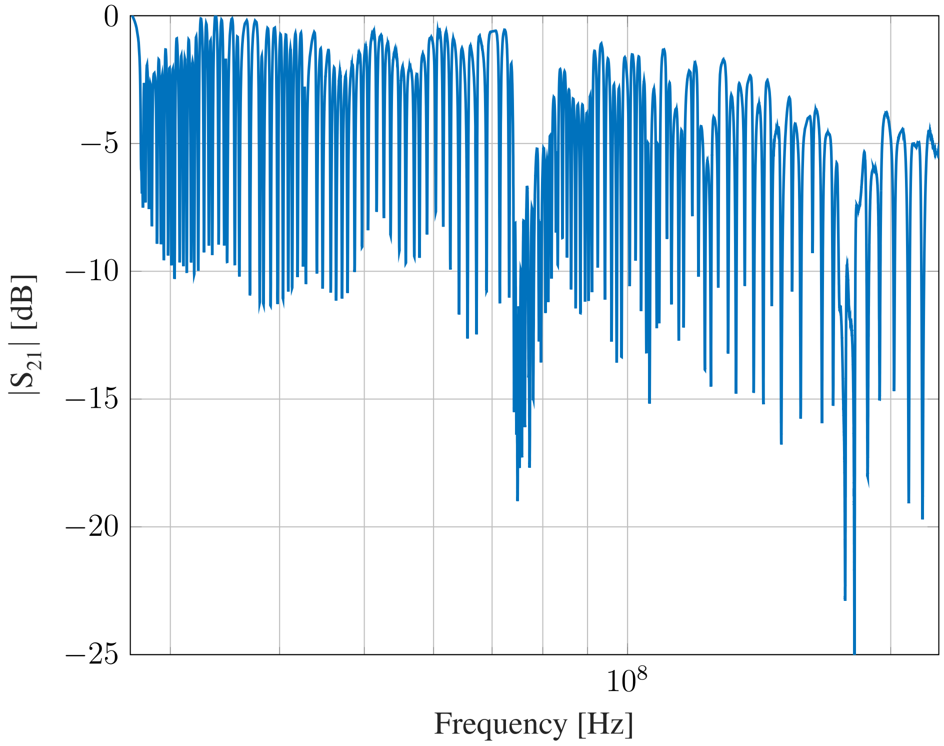

Figure 25. S_{21} of readout channel number 11 at 6.0 K.

7.2.1 Analysis

All in total, over 1000 resonators were measured over the 9 temperature points. The quality factor and the resonant frequency of each resonator were fitted by using a peak finding algorithm to isolate each resonance peak from the measured S_{21} data and then fitted with the resonator model according to Eq. (34). However, this is an idealized model. To further improve the accuracy, the more advanced model in Eq. (46) was used, as described in [58]

$$S_{21} = V_{ext}\left(1 + \alpha\frac{f - f_r}{f_r}\right)\left(1 - \frac{\frac{Q_l}{|Q_e|}e^{i\theta}}{1 + 2iQ_l\frac{f-f_r}{f_r}}\right)e^{i(\phi_v f + \phi_0)} \tag{46}$$

where V_{ext} is the transmission amplitude away from the resonance, f the measured frequency, f_r the resonance frequency, Q_l the loaded quality factor, and Q_e the complex-valued external quality factor.

Eq. (46) takes into account several non-idealities, such as both inductive and capacitive coupling and impedance mismatch in the readout transmission line. The parameter α allows for a linear variation in the overall transmission chain in the narrow frequency range around any given resonance and ϕ_v and ϕ_0 account for the propagation delay of the transmission to and from the resonator to the VNA.

The total inductance for each resonator was calculated with Eq. (43) by using the resonant frequency as determined by the fitting model in Eq. (46) and the theoretical values of the shunt and coupling capacitors as determined by the dimensions of each parallel plate capacitor on the wafer and the permittivity of the dielectric. The geometric inductance L_g = 7 nH, which was modelled using finite element analysis, was assumed to be constant for all resonators at all temperatures. According to Eq. (41), L_g can then be subtracted from the calculated total inductance, giving us the kinetic inductance.

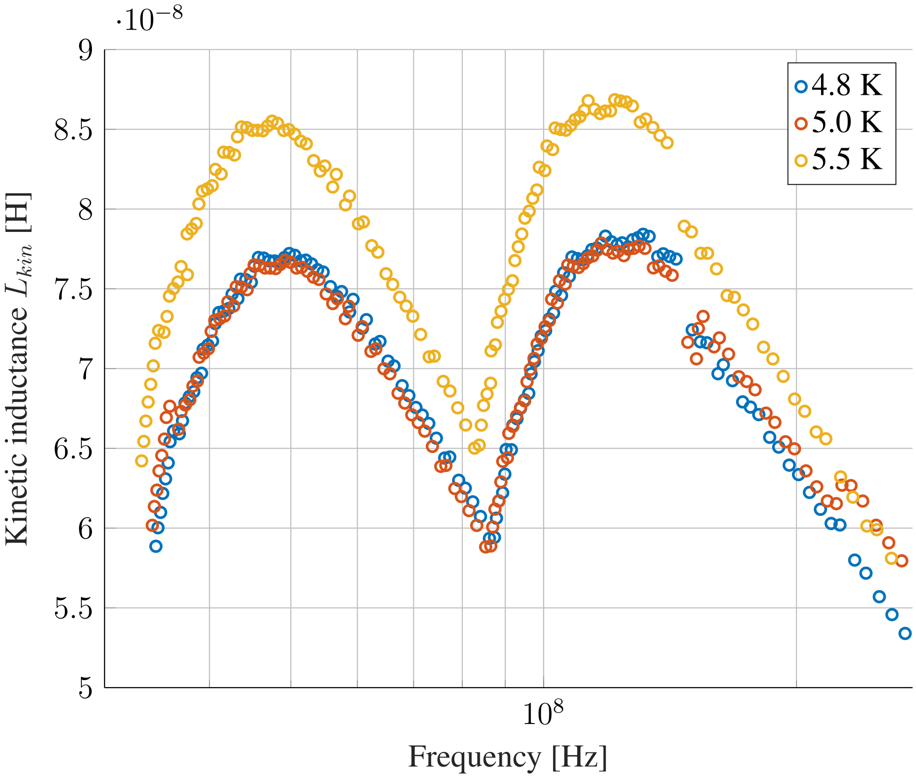

Figure 26. The kinetic inductance L_{kin} of the resonators in the readout channel 1 as a function of the resonance frequency f_r.

As can be seen from Fig. 26, the kinetic inductance has variability over the frequency span, where a dip can be seen at the start, between 50 and 100 MHz and at the end of the spectrum. This is due to imperfections in manufacturing. The dips correspond to resonators at the edges of the wafer, indicating a geographical dependency of the kinetic inductance, caused by for example variations in the thickness of the superconducting film or variability in the capacitance of the shunt and coupling capacitors. Similar geographical dependence was also discovered in [44].

To accurately determine the kinetic inductance as function of temperature, only the lowest and highest resonators in each channel were chosen, as they can be easily identified and associated with a constant capacitance value. This data was then fitted with a modified version of the two-fluid model. The modification was necessary to describe an exact fit with the data and allow the extraction of the parameters for $L_{kin}(0)$ and T_c (Eq. (47)) [43].

$$L(T) = L_{kin}(0)\left[1 - \left(\frac{T}{T_c}\right)^{\alpha}\right]^{-1} + L_g \tag{47}$$

This was then compared to the data provided by the theoretical predictions given by the ideal two-fluid (with α = 4) and Mattis-Bardeen models, using Eqs. (17), (21) and, (41) and by using the data from the T_c measurements as the constants.

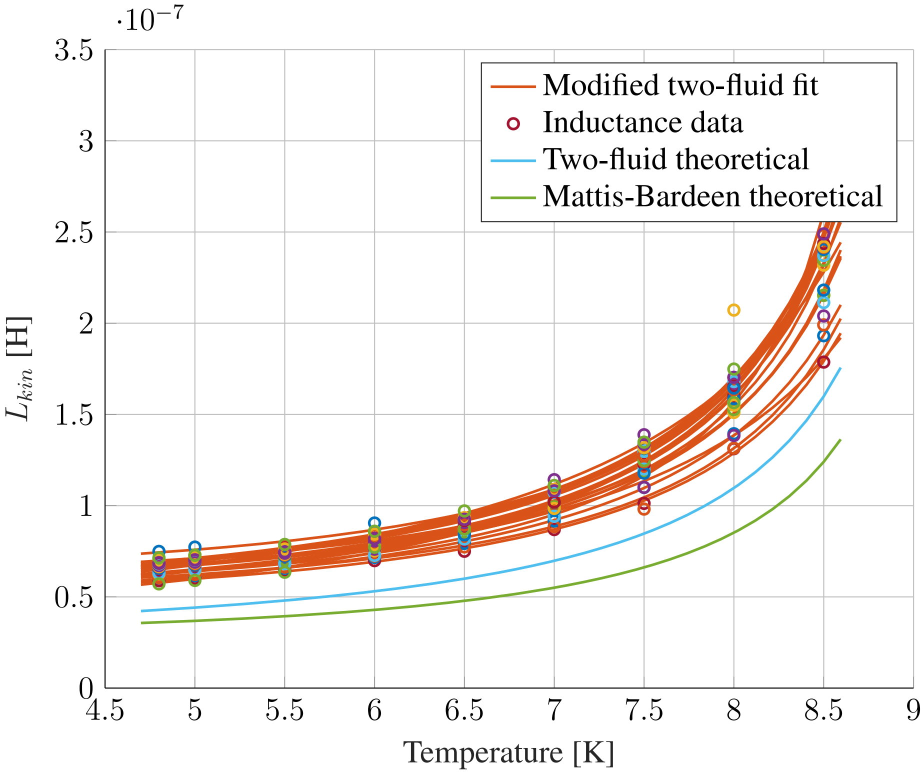

Figure 27. The temperature dependency of the kinetic inductance L_{kin} of all readout channels. The fits according to Eq. (47) are displayed in red. The theoretical values for the kinetic inductances provided by the two-fluid and the Mattis-Bardeen models (Eqs.(41) and (17)).

The average parameters obtained from the fit across all the measured channels are presented in Table 5 and the plots can be seen in Fig. 27.

With the kinetic inductance data, both the two-fluid model and the Mattis-Bardeen model describe the temperature dependency of the inductance appropriately. However, in our particular case, the two-fluid model seems to produce values closer to the experimentally observed data. An offset in the predicted L_{kin} values is expected, as the absolute value of the inductance has significant uncertainty, as the capacitance values used to calculate the inductance are purely based on the theoretical design values and can also have geographical variability over the wafer.

The fitted value for the coefficient α is in agreement with the value observed in the previous generation of the detector utilizing similar NbN films [43].

Table 5. The parameters of the kinetic inductance as extracted from the fitted model in Eq. (47).

$L_{kin}(0)$	T_c	α
52.55 nH	9.50 K	2.45

The fitted T_c deviates from the exact T_c as measured in section 7.1, which suggests the measured data is not fully described by the modified two-fluid model (47) at temperatures close to T_c. It is possible that the mismatch could be partially explained with the differences in film quality over the wafer.

Next, the analysis was continued with the quality factor data obtained from the resonator fits.

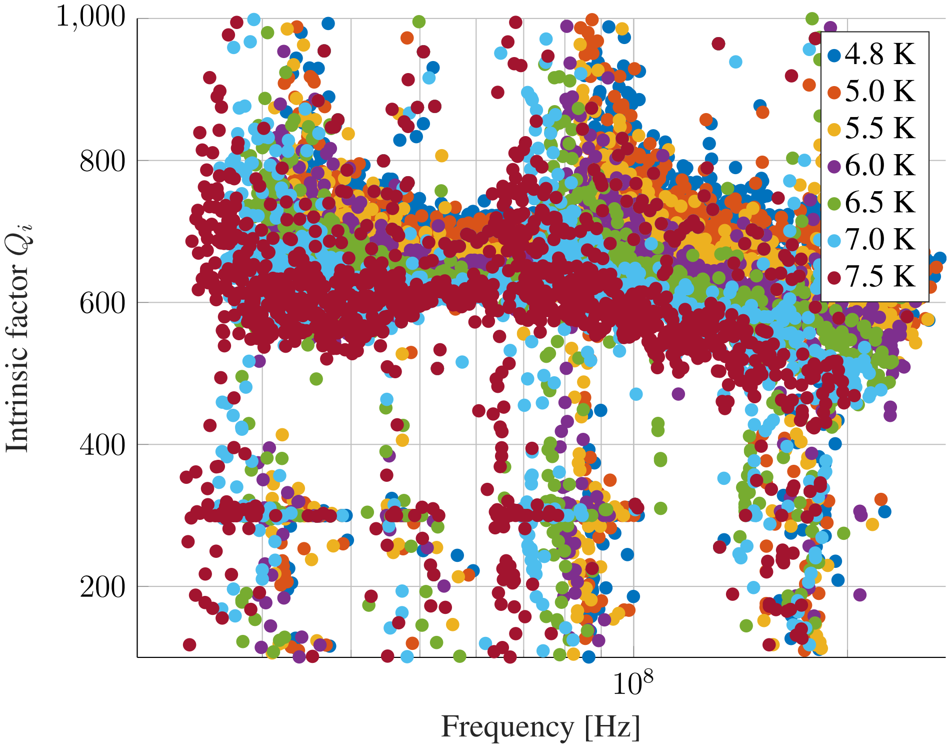

Figure 28. The intrinsic quality factor Q_i of the resonators of all readout channels as a function of the resonance frequency f_r at 4.8 - 7.5 K.

Due to the nature of the fitting algorithm and the close packing of the resonance frequency of each resonator, the algorithm suffers from occasional instability, causing the quality factor spectrum to be quite noisy, especially for the coupling quality factor Q_c. The outlying resonators were manually removed from the data.

For the KIB resonators, the intrinsic quality factor (as described for general RLC resonator in Eq. (28)) takes the form [59]

$$Q_i = \frac{\omega_r L_s}{\frac{L_{kin}}{L_{tot}} R_s} \approx \frac{\sigma_2}{\frac{L_{kin}}{L_{tot}} \sigma_1} \tag{48}$$

where $L_s = \frac{\mu_0 \lambda^2}{t}$ is the surface inductance and $R_s \approx \sigma_1/(d\sigma_2^2)$ the surface resistance.

As the surface conductivity of the film is defined by the Mattis-Bardeen theory, Q_i can be calculated by solving the integrals in appendix 1 with the appropriate initial conditions. This was done numerically using the parameters measured in section 7.1, and the results are presented in Fig. 29.

The intrinsic quality factor has only a small dependence on the frequency, as seen at the higher frequencies in Fig. 28. The inverse frequency dependence of the quality factor, as observed in [44] and characteristic for superconductor losses, could not be seen in the data from these measurements.

For fitting the temperature dependency of the quality factor, quality factor data was chosen from the least noisy section of the data, i.e., the frequency range of 50 - 70 MHz at 6.0K, and averaged between all channels. The obtained data is presented in Table 6.

Table 6. The average intrinsic quality factors Q_i of all measured channels at 8 temperature points.

Temperature	Q_i
4.8 K	706.9
5.0 K	691.6
5.5 K	667.4
6.0 K	649.1
6.5 K	635.2
7.0 K	628.9
7.5 K	620.1
8.0 K	616.4

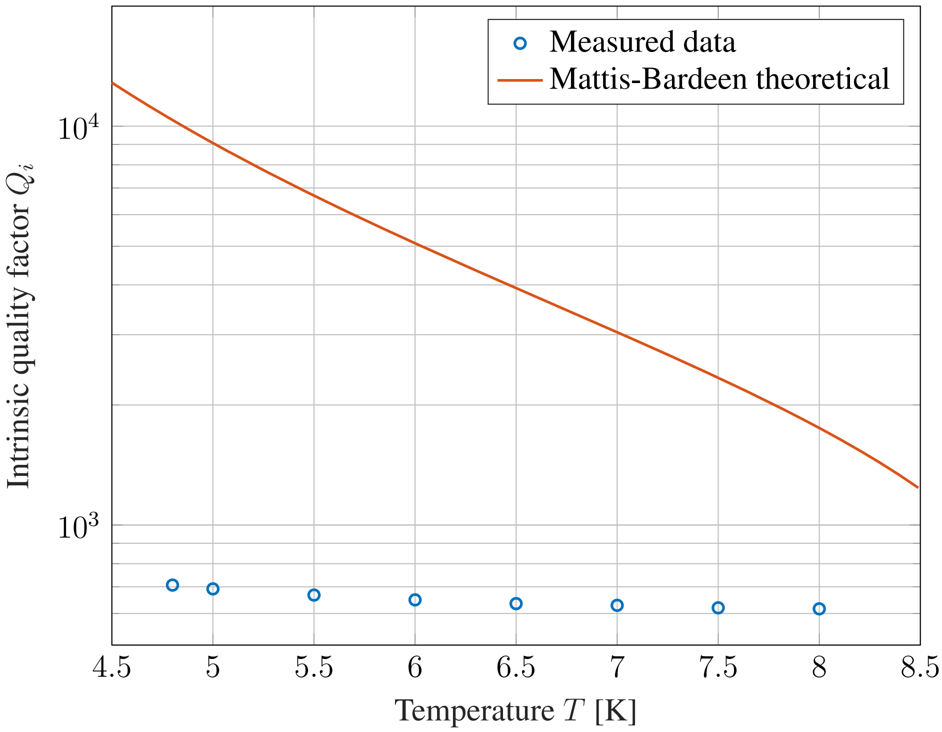

Figure 29. The temperature dependency of the averaged intrinsic quality factors of all measured channels and the Mattis-Bardeen theoretical values.

The observed temperature dependence does not follow the predictions of the two-fluid model, as the losses and therefore the quality factor are proportional to the population of quasiparticles (Eq. (4)), meaning that the Mattis-Bardeen model must be utilized to describe the observations. The theoretical values for Q_i from the Mattis-Bardeen theory predicts a quality factor significantly higher than observed, but the line shape matches the data. The loss of quality factors can be explained with excess loss mechanisms in the resonators, obscuring both the predicted frequency and temperature dependency [60]. Further analysis is needed to investigate their contributions.

7.3 Thermal cut-off measurements

The noise characteristics of the imaging system and thermal cut-off frequency were measured by utilizing a NIST aquatic blackbody calibrator [61] as a terahertz radiation source. The water bath temperature of the calibrator was controlled using a Polyscience temperature controller and set to a constant 30 °C. To produce a reference signal, the blackbody thermal signal is modulated by an Oriel optical chopper. Then, the power spectral density (PSD) is extracted from the time domain data of the readout electronics by using Fourier analysis. The measurement setup is depicted in Fig. 30.

Figure 30. The noise measurement setup with the LASTKID instrument is visible on the left, the blackbody calibrator and the optical chopper on the right.

Four detectors were picked out on the focal plane, which corresponded to about 10 cm in length on the image plane and were able to fit inside the blade diameter of the chopper. The measurement was carried out by using the readout electronics of the imaging system itself, for which the excitation parameters were selected by hand, as described in section 6.4.

To determine the thermal cut-off frequency of the detector, caused by the heat capacitance and thermal conductance of the bolometer, the chopping frequency f_{ch} was swept from 40 Hz to 130 Hz (limited by the maximum frequency of the chopper) as the time data was recorded from the chosen four detectors over the period of approximately 30 seconds at the sampling interval of 60 µs.

7.3.1 Analysis

From the time domain signals recorded by the readout electronics, a MATLAB script was used to perform Fourier transforms to produce the PSDs of the signals. The PSD was averaged 25 times to smooth the spectrum. The 1 Hz signal caused by the temperature oscillations from the pulse tube was removed from the spectrum, along with its harmonics.

To obtain the signal, the signal peak in the PSD at the chopping frequency was numerically integrated. At the thermal cut-off frequency, the signal should be down -3 dB from its baseline level. However, over the swept chopping frequency range, we could not observe a clear plateau nor the -3 dB drop in the signal amplitude. This is likely caused by the slow temperature drifts misaligning the detector resonance from its stimulus frequency and narrow chopping frequency band under study. The signal magnitudes are plotted in Fig. 31.

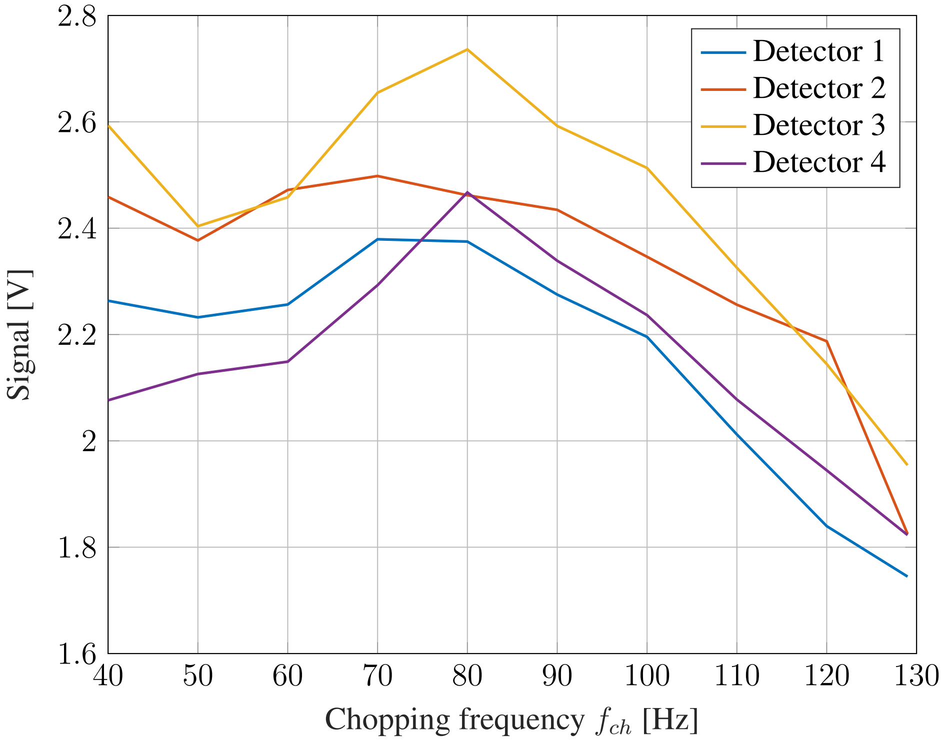

Figure 31. The integrated signal amplitude as a function of the chopping frequency.

In failing to directly measure the thermal cut-off frequency, efforts were made to determine the thermal cut-off from the spectral data. Assuming that the phonon noise in the bolometer is the dominant noise source, we should see a roll-off in the noise signal at the thermal cut-off frequency of the bolometer, as the phonon noise is effectively filtered from the bolometer by the thermal time constant. This cut-off response was modelled and the frequency was estimated by hand to best fit the data from the measurements. The result is presented in the Fig. 32, where the cut-off frequency has been set to 100 Hz, the phonon noise level to 27 mV/Hz$^{1/2}$ and the white noise level to 6 mV/Hz$^{1/2}$. This seems to provide a satisfactory fit.

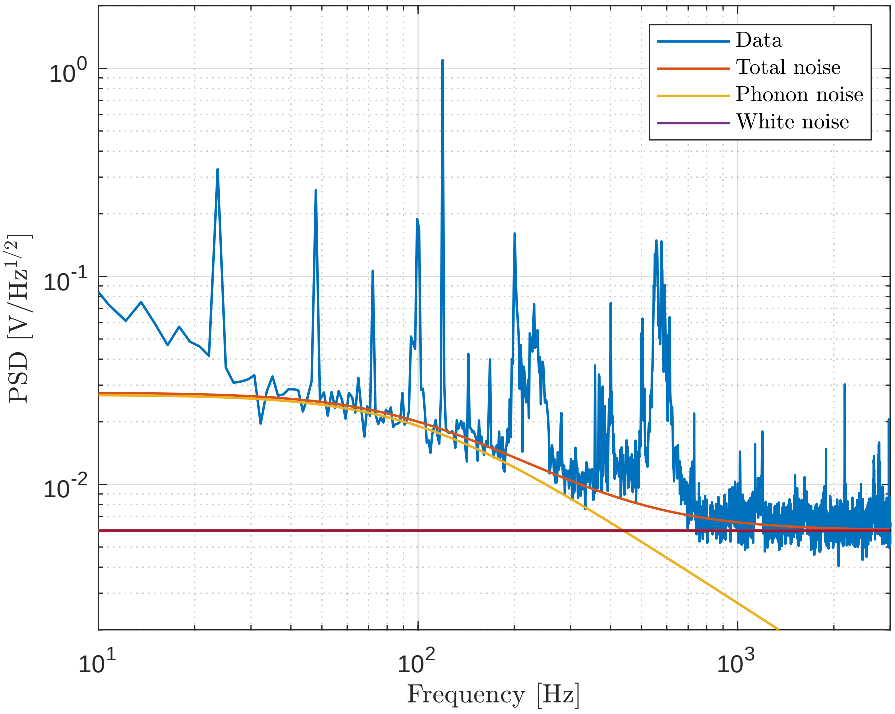

Figure 32. By-hand estimation of the thermal cut-off frequency from the spectral data, where the chopper signal is visible as a peak at 120 Hz.

7.4 Imaging experiments

Additionally, some imaging experiments were performed to demonstrate the imaging capabilities of the LASTKID system, published in [51]. Snapshots of a video image are shown in Fig. 33. To demonstrate the concealed item detection capabilities of LASTKID, plastic rods made from polyoxymethylene (POM) of diameters 30 mm and 16 mm were hidden under the imaging subject's hooded cotton shirt. Multiple videos were recorded to demonstrate the spatial resolution capabilities.

The detector readout was tuned as described in section 6.4, providing the excitation parameters and the encoding of the detector eigenfrequencies into the corresponding spatial coordinates. Two dead rows of pixels were observed, caused by defective readout channel electronics.

For video recording, the mechanical chopper was set to 37 Hz while the data was recorded simultaneously from 20 readout channels, corresponding to a total detector count of 2280 and an imaging area of 86 x 66 cm^2. SAFE slot time τ_S was adjusted to 60 µs, leading to a frame time τ_F = 6.8 ms for N = 114 detectors in each channel. Finally, videos were produced using gamma correction with an exponent of 2.32 for colour scale.

A 16 mm wide rod can be recognized under the shirt, and also other features such as the nose of the test person are distinguishable in the videos.

The results demonstrate the performance of the fully staring imaging system for concealed object detection at the spatial resolution of 16 mm and with sufficient sensitivity. The data is in line with the characteristics and radiometric contrast measurements presented in previous work [50, 53].

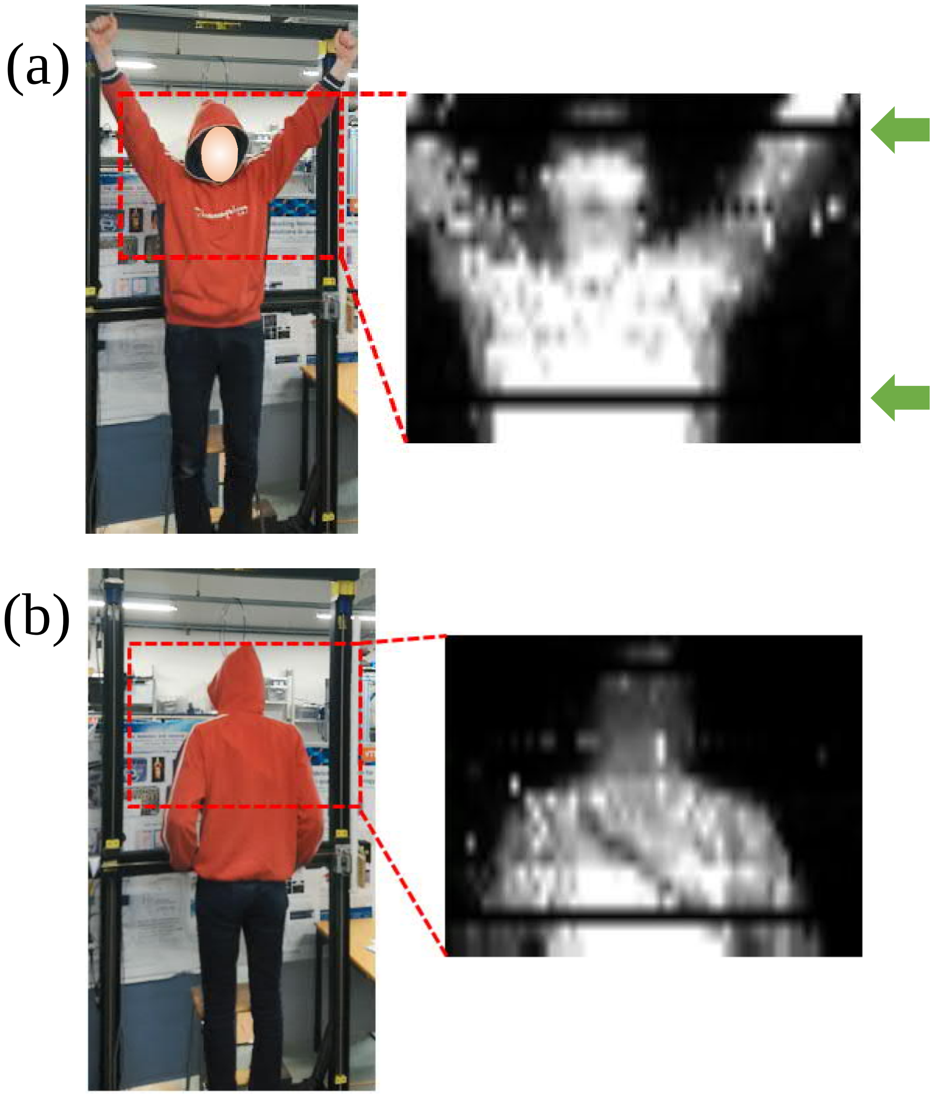

Figure 33. Resulting images from the experiment. Reference photographs are included. The two dead rows of pixels are identified with arrows. In (b) the 16 mm POM rod is visible under the shirt in the THz image [51].

8 DISCUSSION

8.1 Current study

The thin film measurements were largely a success, even though a defective bond wire prevented a four-terminal measurement of one sample. At first, the cryostat was suffering from thermal leakage issues, which caused some instabilities in the temperature control. These problems were eventually solved, enabling the determination of T_c of NbN films.

The quality factors and resonant frequencies of the KIB resonators were successfully measured. To fully characterize the electrodynamics of the KIBs, a more thorough exploration of the resonator loss model is in order, as the observed excess loss can occur through several mechanisms [60].

The measurements aiming to determine thermal response of the bolometer suffered from external interference and thermal drifts present in the setup, degrading the quality of the measurement data. These issues should be addressed in future experiments. Also, the use of an external heater mounted on the membrane to create a stronger signal for the measurements should be considered.

The imaging experiments were successful at demonstrating LASTKIDs imaging capabilities, although the utilization of the full focal plane array was not implemented.

8.2 Future work

In this thesis, effort was put into characterizing electrical and thermal parameters of KIB. These parameters then determine the detector performance through quantities such as noise, responsivity (Eq. (44)), speed and dynamic range, which in turn impact the performance of the whole imaging system. Further work is needed to fully understand the mechanisms behind the low quality factors measured. Also understanding thermal properties of the bolometer, i.e., heat capacitance and thermal conductance, is crucial for determining the optimal detector design. This data will shed light on material properties such as thermal conductivity and specific heat capacity, for which low temperature data is not readily available. Also, developing thermal circuit models for bolometers will help one to understand the detector performance in more detail.

To fully characterize the resonator variability over the wafer, a more thorough examination of the measurement data should be conducted with a method to link each resonator to correct spatial coordinates on the focal plane. The data gathered during this thesis provides a good basis for such research.

Iterative optimization of the current detector design is in progress. To further increase the sensitivity, detectors with smaller membrane size have been designed and are being fabricated. To compensate for the reduced absorbing area, the optical coupling is improved by introducing a lens-coupled bolometer design.

Although glossed over in this thesis, modelling of transmission line coupled resonators is by no means a trivial task. Even though accounting for many alterations to the data in the real measurement scenario, it has been suggested that the accuracy of the resonator model depicted in [58] could be improved. Developing the resonator model and fitting routines further according to the fitting methods suggested by [62] could lead to more accurate parameter extraction and error estimation. Another path to explore would be to model the resonators as Fano resonances, due to their proximity in the frequency spectrum [63].

In this thesis, the KIBs were operated purely in the linear regime, where the heating caused by the applied readout power was well below being significant. It has been suggested that the NEP of the detectors could be optimized by carefully tuning the readout power and the operating point of the detectors [64]. Therefore, exploring the nonlinear operation regime could be a worthwhile effort. The drawback of the increased responsivity obtained from the higher readout power and nonlinear regime is reduction in the dynamic range of the detector [59].

The imaging software is currently in its infancy. All the calibration processes for setting the phase references and the excitation signal frequencies need to be done manually by using external scripts for calculation, which takes a considerable amount of time. Similarly, the video images have to be rendered by using separate scripts on the captured data, meaning that no images can be observed in real-time. The development of a fully integrated software for calibration and imaging would make operating the imaging system significantly quicker and easier, and provide the ability of real-time imaging.

So far, reliability issues related to the readout electronics have prevented the use of the whole focal plane array and thus hindered the demonstration of imaging with the full field of view of the instrument (1 x 2 m^2).

9 CONCLUSION

The superconducting parameters of the niobium nitride thin films were determined. The average critical temperature of the films was 10.4 K and the average room temperature resistivity 621 µΩcm. From these values, the gap energy $\Delta(0)$ was calculated to be 1.58 meV and the penetration depth at zero temperature $\lambda(0)$ to be approximately 800 nm.

Transmission measurements of the focal plane array of kinetic inductance bolometers were conducted. Based on the measurement, the resonator parameters of the collocated RLC resonators were determined. The kinetic inductance and quality factor of the resonators were calculated as a function of temperature. The average kinetic inductance $L_{kin}(0)$ for the KIBs was estimated as 53 nH. The average intrinsic quality factor Q_i at the lowest measured temperature point of 4.8 K was in the order of 700. The temperature data was compared to the predictions of the two-fluid and Mattis-Bardeen models, with measurements providing higher values for kinetic inductance than theoretically estimated. The numerically solved Mattis-Bardeen integrals predict significantly higher intrinsic quality factors for the resonators than measured in the experiment, indicating excess loss mechanisms.

The direct measurements utilizing the signal of the blackbody source were not conclusive in determining the thermal cut-off frequency, but this was estimated in turn from the detector noise spectrum to be approximately 100 Hz, by fitting best-match curves for the phonon noise and white noise floor of the system with values of 26 mV/Hz$^{1/2}$ and 6 mV/Hz$^{1/2}$ respectively.

Also, imaging experiments were conducted and the performance of the imaging system was verified in a practical imaging scenario.

10 SUMMARY

In this thesis, the passive terahertz imaging system LASTKID was introduced, along with the basics of terahertz technology and applications. An overview of terahertz imaging technology was given. The theory of operation of the kinetic inductance bolometers utilized in LASTKID was introduced by reviewing the physics of superconductivity, radio frequency resonators and bolometers. Three experiments were conducted to characterize the superconductor parameters, the resonator parameters, thermal response and noise characteristics of LASTKID. In a fourth experiment, LASTKID was used to perform imaging experiments to demonstrate its performance for concealed item detection.

REFERENCES

[1] Asqella Oy, Finland. https://asqella.com/, 2020. [Online; accessed May, 19, 2020].

[2] Jae-Sung Rieh. *Introduction to Terahertz Electronics*. Springer International Publishing, 2021.

[3] Alex Svetlitza, Michael Slavenko, Tatiana Blank, Igor Brouk, Sara Stolyarova, and Yael Nemirovsky. Thz measurements and calibration based on a blackbody source. *IEEE Transactions on Terahertz Science and Technology*, 4(3):347–359, 2014.

[4] Thomas Dillon, Christopher Schuetz, Richard Martin, E Stein, Jesse Samluk, Daniel Mackrides, Mark Mirotznik, and Dennis Prather. Optical configuration of an upconverted millimeter-wave distributed aperture imaging system. *Proceedings of SPIE - The International Society for Optical Engineering*, 7485, 09 2009.

[5] D. J. Fixsen, E. S. Cheng, J. M. Gales, J. C. Mather, R. A. Shafer, and E. L. Wright. The cosmic microwave background spectrum from the full cobe/firas data set. *The Astrophysical Journal*, 473(2):576587, Dec 1996.

[6] Yihong Yang, Alisha Shutler, and D Grischkowsky. Measurement of the transmission of the atmosphere from 0.2 to 2 thz. *Optics express*, 19:8830–8, 04 2011.

[7] Ali Rostami, Hassan Rasooli, and Hamed Baghban. *Terahertz Technology*. Springer Berlin Heidelberg, 2011.

[8] P. A. R. Ade, N. Aghanim, M. I. R. Alves, C. Armitage-Caplan, M. Arnaud, M. Ashdown, F. Atrio-Barandela, J. Aumont, H. Aussel, and et al. Planck2013 results. i. overview of products and scientific results. *Astronomy & Astrophysics*, 571:A1, Oct 2014.

[9] Planck and the cosmic microwave background, The European Space Agency. https://www.esa.int/Science_Exploration/Space_Science/Planck/Planck_and_the_cosmic_microwave_background. [Online; accessed August, 4, 2021].

[10] H. Elayan, O. Amin, R. M. Shubair, and M. Alouini. Terahertz communication: The opportunities of wireless technology beyond 5g. In *2018 International Conference on Advanced Communication Technologies and Networking (CommNet)*, pages 1–5, 2018.

[11] Hironori Matsumoto, Issei Watanabe, Akifumi Kasamatsu, and Yasuaki Monnai. Integrated terahertz radar based on leaky-wave coherence tomography. *Nature Electronics*, 3(2):122–129, Feb 2020.

[12] Changzhi Li, Victor M. Lubecke, Olga Boric-Lubecke, and Jenshan Lin. A review on recent advances in doppler radar sensors for noncontact healthcare monitoring. *IEEE Transactions on Microwave Theory and Techniques*, 61(5):2046–2060, 2013.

[13] Sequestim, Finland. https://sequestim.com/technology/, 2021. [Online; accessed July, 22, 2021].

[14] Yun-Shik Lee. *Principles of Terahertz Science and Technology*. Springer Publishing Company, Incorporated, 1st edition, 2008.

[15] R. Appleby and H. B. Wallace. Standoff detection of weapons and contraband in the 100 ghz to 1 thz region. *IEEE Transactions on Antennas and Propagation*, 55(11):2944–2956, 2007.

[16] Samuel Rowe. *Passive terahertz imaging with lumped element kinetic inductance detectors*. PhD thesis, Cardiff University, 2015.

[17] A Shurakov, Y Lobanov, and G Goltsman. Superconducting hot-electron bolometer: from the discovery of hot-electron phenomena to practical applications. *Superconductor Science and Technology*, 29(2):023001, dec 2015.

[18] W. Zhang, W. Miao, K. M. Zhou, X. H. Guo, J. Q. Zhong, and S. C. Shi. High sensitive THz superconducting hot electron bolometer mixers and transition edge sensors. In Cunlin Zhang, Xi-Cheng Zhang, and Masahiko Tani, editors, *Infrared, Millimeter-Wave, and Terahertz Technologies IV*, volume 10030, pages 7 – 14. International Society for Optics and Photonics, SPIE, 2016.

[19] S. Doyle, P. Mauskopf, J. Naylon, A. Porch, and C. Duncombe. Lumped element kinetic inductance detectors. *Journal of Low Temperature Physics*, 151(1):530–536, Apr 2008.

[20] Albert Wandui, James J. Bock, Clifford Frez, M. Hollister, Lorenzo Minutolo, Hien Nguyen, Bryan Steinbach, Anthony Turner, Jonas Zmuidzinas, and Roger OBrient. Thermal kinetic inductance detectors for millimeter-wave detection. *Journal of Applied Physics*, 128(4):044508, 2020.

[21] J. E. Sauvageau and D. G. McDonald. Superconducting kinetic inductance bolometer. *IEEE Transactions on Magnetics*, 25(2):1331–1334, 1989.

[22] A. Luukanen, H. Haimakainen, and P. Kajatkari. Full-body submillimeter-wave thermography for counter-pandemic applications. In David A. Wikner and Duncan A. Robertson, editors, *Passive and Active Millimeter-Wave Imaging XXIV*, volume 11745, pages 110 – 117. International Society for Optics and Photonics, SPIE, 2021.

[23] Dirk van Delft and Peter Kes. The discovery of superconductivity. *Physics Today*, 63(9):38–43, 2010.

[24] W. Meissner and R. Ochsenfeld. Ein neuer effekt bei eintritt der supraleitfähigkeit. *Die Naturwissenschaften*, 21(44):787–788, November 1933.

[25] M. Tinkham. *Introduction to Superconductivity*. Dover Books on Physics Series. Dover Publications, 2004.

[26] C. Kittel. *Introduction to Solid State Physics*. Wiley, 1996.

[27] C Jo Gorter and H Casimir. The thermodynamics of the superconducting state. *Z. tech. Phys*, 15:539–42, 1934.

[28] Theodore Duzer. *Principles of superconductive devices and circuits*. Prentice Hall, Upper Saddle River, N.J, 1999.

[29] F. London and H. London. The electromagnetic equations of the supraconductor. *Proceedings of the Royal Society of London. Series A - Mathematical and Physical Sciences*, 149(866):71–88, March 1935.

[30] Simon Doyle. *Lumped element Kinetic Inductance Detectors*. PhD thesis, Cardiff University, 2008.

[31] J. Bardeen, L. N. Cooper, and J. R. Schrieffer. Microscopic theory of superconductivity. *Phys. Rev.*, 106:162–164, Apr 1957.

[32] J. Bardeen, L. N. Cooper, and J. R. Schrieffer. Theory of superconductivity. *Phys. Rev.*, 108:1175–1204, Dec 1957.

[33] Bernhard Mühlschlegel. Die thermodynamischen funktionen des supraleiters. *Zeitschrift für Physik*, 155(3):313–327, June 1959.

[34] D. C. Mattis and J. Bardeen. Theory of the anomalous skin effect in normal and superconducting metals. *Phys. Rev.*, 111:412–417, Jul 1958.

[35] Rebecca Ann Wernis. *Characterizing a Resonator Bolometer Array*. PhD thesis, California Institute of Technology, 2013.

[36] David M Pozar. *Microwave engineering; 3rd ed.* Wiley, Hoboken, NJ, 2005.

[37] Peter Barry. *On the development of SuperSpec: a fully integrated on-chip spectrometer for far-infrared astronomy*. PhD thesis, Cardiff University, 2014.

[38] S. P. Langley. The bolometer and radiant energy. *Proceedings of the American Academy of Arts and Sciences*, 16:342–358, 1880.

[39] R. Kokkoniemi, J.-P. Girard, D. Hazra, A. Laitinen, J. Govenius, R. E. Lake, I. Sallinen, V. Vesterinen, M. Partanen, J. Y. Tan, K. W. Chan, K. Y. Tan, P. Hakonen, and M. Möttönen. Bolometer operating at the threshold for circuit quantum electrodynamics. *Nature*, 586(7827):47–51, Oct 2020.

[40] P. L. Richards. Bolometers for infrared and millimeter waves. *Journal of Applied Physics*, 76(1):1–24, 1994.

[41] John C. Mather. Bolometer noise: nonequilibrium theory. *Appl. Opt.*, 21(6):1125–1129, Mar 1982.

[42] Juha Hassel, Andrey V. Timofeev, Visa Vesterinen, Hannu Sipola, Panu Helistö, Mika Aikio, Aki Mäyrä, Leif Grönberg, and Arttu Luukanen. Bolometric kinetic inductance detector technology for sub-millimeter radiometric imaging. In Neil A. Salmon and Eddie L. Jacobs, editors, *Millimetre Wave and Terahertz Sensors and Technology VIII*, volume 9651, pages 101 – 107. International Society for Optics and Photonics, SPIE, 2015.

[43] Andrey V Timofeev, Visa Vesterinen, Panu Helistö, Leif Grönberg, Juha Hassel, and Arttu Luukanen. Submillimeter-wave kinetic inductance bolometers on free-standing nanomembranes. *Superconductor Science and Technology*, 27(2):025002, dec 2013.

[44] A. Timofeev, J. Luomahaara, L. Grönberg, A. Mäyrä, H. Sipola, M. Aikio, M. Metso, V. Vesterinen, K. Tappura, J. Ala-Laurinaho, A. Luukanen, and J. Hassel. Optical and electrical characterization of a large kinetic inductance bolometer focal plane array. *IEEE Transactions on Terahertz Science and Technology*, 7(2):218–224, 2017.

[45] Arttu Luukanen, Markus Grönholm, Petteri Lappalainen, Mikko Leivo, Anssi Rautiainen, Aleksi Tamminen, Juha Ala-Laurinaho, Antti Räisänen, Charles R. Dietlein, and Erich N. Grossman. Passive real-time submillimetre-wave imaging system utilizing antenna-coupled microbolometers for stand-off security screening applications. In *2010 International Workshop on Antenna Technology (iWAT)*, pages 1–4, 2010.

[46] Arttu Luukanen, Juha Ala-Laurinaho, Janne Häkli, David Gomes-Martins, Tero Kiuru, Päivi Koivisto, Mikko Leivo, Anssi Rautiainen, Jussi Säily, Aleksi Tamminen, Hans Toivanen, Reijo Tuovinen, and Antti Räisänen. Towards video rate imaging at submillimetre-waves finnish developments of passive multi-band imaging and holographic submm-wave beam steering at vtt. In *2012 Asia Pacific Microwave Conference Proceedings*, pages 782–784, 2012.

[47] A. Luukanen, L. Grönberg, T. Haarnoja, P. Helistö, K. Kataja, M. Leivo, A. Rautiainen, J. Penttilä, J. E Bjarnason, C. R. Dietlein, M. D. Ramirez, and E. N. Grossman. Passive THz imaging system for stand-off identification of concealed objects: results from a turn-key 16 pixel imager. In Roger Appleby and David A. Wikner, editors, *Passive Millimeter-Wave Imaging Technology XI*, volume 6948, pages 164 – 172. International Society for Optics and Photonics, SPIE, 2008.

[48] A. Luukanen and J. P. Pekola. A superconducting antenna-coupled hot-spot microbolometer. *Applied Physics Letters*, 82(22):3970–3972, 2003.

[49] Arttu R.M. Luukanen and Veli-Pekka Viitanen. Terahertz imaging system based on antenna-coupled microbolometers. In Roger M. Smith, editor, *Passive Millimeter-Wave Imaging Technology II*, volume 3378, pages 34 – 44. International Society for Optics and Photonics, SPIE, 1998.

[50] Juho Luomahaara, Aki Mäyrä, Mika Aikio, Hannu Sipola, Leif Grönberg, Andrey Timofeev, Kirsi Tappura, Anssi Rautiainen, Juha Ala-Laurinaho, Aleksi Tamminen, Visa Vesterinen, Mikko Leivo, Feng Gao, Hannu Vasama, Arttu Luukanen, and Juha Hassel. A fully-staring THz video camera with wide field-of-view and close-looking optics. In Neil A. Salmon and Frank Gumbmann, editors, *Millimetre Wave and Terahertz Sensors and Technology XIII*, volume 11541, pages 7 – 14. International Society for Optics and Photonics, SPIE, 2020.

[51] Juho Luomahaara, Hannu Sipola, Leif Grönberg, Aki Mäyrä, Mika Aikio, Andrey Timofeev, Kirsi Tappura, Anssi Rautiainen, Aleksi Tamminen, Visa Vesterinen, Mikko Leivo, Feng Gao, Hannu Vasama, Arttu Luukanen, and Juha Hassel. A passive, fully staring thz video camera based on kinetic inductance bolometer arrays. *IEEE Transactions on Terahertz Science and Technology*, 11(1):101–108, 2021.

[52] Charles Dietlein, A. Luukanen, Francois Meyer, Zoya Popovic, and Erich Grossman. Phenomenology of passive broadband terahertz images. ESA Workshop on Millimetre-wave Technology and Applications, Espoo, FI, 2006-02-15 2006.

[53] Hannu Sipola, Juho Luomahaara, Andrey Timofeev, Leif Grönberg, Anssi Rautiainen, Arttu Luukanen, and Juha Hassel. Multiplexed readout of kinetic inductance bolometer arrays. *Review of Scientific Instruments*, 90(7):074702, 2019.

[54] L. J. Swenson, P. K. Day, B. H. Eom, H. G. Leduc, N. Llombart, C. M. McKenney, O. Noroozian, and J. Zmuidzinas. Operation of a titanium nitride superconducting microresonator detector in the nonlinear regime. *Journal of Applied Physics*, 113(10):104501, Mar 2013.

[55] Alexander Podzorov and Guilhem Gallot. Low-loss polymers for terahertz applications. *Appl. Opt.*, 47(18):3254–3257, Jun 2008.

[56] Carole E. Tucker and Peter A. R. Ade. Thermal filtering for large aperture cryogenic detector arrays. In Jonas Zmuidzinas, Wayne S. Holland, Stafford Withington, and William D. Duncan, editors, *Millimeter and Submillimeter Detectors and Instrumentation for Astronomy III*, volume 6275, pages 239 – 247. International Society for Optics and Photonics, SPIE, 2006.

[57] Dominic J. Benford, Michael C. Gaidis, and Jacob W. Kooi. Optical properties of zitex in the infrared to submillimeter. *Appl. Opt.*, 42(25):5118–5122, Sep 2003.

[58] A. Bruno, G. de Lange, S. Asaad, K. L. van der Enden, N. K. Langford, and L. DiCarlo. Reducing intrinsic loss in superconducting resonators by surface treatment and deep etching of silicon substrates. *Applied Physics Letters*, 106(18):182601, 2015.

[59] Visa Vesterinen. *Microwave-coupled superconducting devices for sensing and quantum information processing*. Doctoral thesis, Aalto University, 2015.

[60] C. R. H. McRae, H. Wang, J. Gao, M. R. Vissers, T. Brecht, A. Dunsworth, D. P. Pappas, and J. Mutus. Materials loss measurements using superconducting microwave resonators. *Review of Scientific Instruments*, 91(9):091101, 2020.

[61] Charles Dietlein, Zoya Popović, and Erich N. Grossman. Aqueous blackbody calibration source for millimeter-wave/terahertz metrology. *Appl. Opt.*, 47(30):5604–5615, Oct 2008.

[62] Giuseppe Cataldo, Edward J. Wollack, Emily M. Barrentine, Ari D. Brown, S. Harvey Moseley, and Kongpop U-Yen. Analysis and calibration techniques for superconducting resonators. *Review of Scientific Instruments*, 86(1):013103, Jan 2015.

[63] J. M. Hornibrook, E. E. Mitchell, and D. J. Reilly. Superconducting resonators with parasitic electromagnetic environments, 2012.

[64] T Guruswamy, C N Thomas, S Withington, and D J Goldie. Electrothermal feedback in kinetic inductance detectors. *Superconductor Science and Technology*, 30(6):064006, may 2017.

Appendix 1. Mattis-Bardeen integrals

Here σ_1 and σ_2 are the same as in Eq. (3). The normal state conductivity σ_n is defined as the conductivity just above the critical temperature T_c

$$\frac{\sigma_1}{\sigma_n} = \frac{1}{\hbar\omega}\int_{\Delta}^{\infty} \left[f(E) - f(E-\hbar\omega)\right] g(E)\, dE + \frac{2}{\hbar\omega}\int_{\Delta-\hbar\omega}^{\Delta} \left[1 - 2f(E+\hbar\omega)\right] g(E)\, dE \tag{49}$$

$$\frac{\sigma_2}{\sigma_n} = \frac{1}{\hbar\omega}\int_{\Delta-\hbar\omega,-\Delta}^{\Delta} \frac{\left[1 - 2f(E-\hbar\omega)\right]\left(E^2 + \Delta^2 + \hbar\omega E\right)}{\left(\Delta^2 - E^2\right)^{\frac{1}{2}}\left[(E+\hbar\omega)^2 - \Delta^2\right]^{\frac{1}{2}}}\, dE \tag{50}$$

where $f(\varepsilon)$ is the Fermi function

$$f(\varepsilon) = \frac{1}{1 + \exp\left(\varepsilon/k_B T\right)} \tag{51}$$

and

$$g(E) = \frac{E^2 + \Delta^2 + \hbar\omega E}{\left(E^2 - \Delta^2\right)^{\frac{1}{2}}\left[(E+\hbar\omega)^2 - \Delta^2\right]^{\frac{1}{2}}} \tag{52}$$